APPLIED SCIENCES AND ENGINEERING

Microenvironment-driven transformable self-assembly nanoplatform enables spatiotemporal remodeling for rheumatoid arthritis therapy

Chuan Hu[1]†, Jiaqi Ma[1]†, Xi Chen[1], Yaxin Chen[1], Yujun Song[2], Qingsong Tang[1], Xinling He[1], Yitao Wang[1,3], Huile Gao[2]*, Jinming Zhang[1]*

The aberrant vasculature within the inflamed joint cavity of rheumatoid arthritis (RA) not only exacerbates joint pathology but also restricts the effective delivery of therapeutic drugs. Herein, we propose a strategy that involves the rapid and sustained vasculature repair alongside microenvironment-driven drug delivery to achieve multifaceted RA management. The transformable, self-assembling nanoplatform specifically accumulates in the inflamed joint cavity guided by a vascular targeting peptide (STP). Subsequently, STP detaches and undergoes shape transformation, forming nanofibers on the vascular endothelium, which serve as a rapid-acting physical barrier in the short term and facilitate sustained vascular normalization in the long term. Concurrently, the remaining nanoparticles undergo charge reversal and RGD exposure, enabling precise delivery of anti-RA agent triptolide and the immunomodulatory agent metformin. Collectively, this study provides a potent strategy for rapid, sustained, and precise spatiotemporal remodeling of RA using a simple yet intelligent self-assembling nanoplatform.

INTRODUCTION

Rheumatoid arthritis (RA) is an autoimmune disease primarily characterized by joint inflammation and immune abnormalities. Several traditional therapeutic options, such as nonsteroidal anti-inflammatory drugs, glucocorticoids, and natural components [triptolide (TPL)], mainly alleviate inflammation or have limited immunomodulation effects, showing insufficient therapeutic efficacy (*1*–*5*). Throughout the progression of RA, vascular abnormalities play a notable role, not only promoting synovial hyperplasia and bone destruction but also contributing to the recruitment of additional inflammatory immune cells. This occurs as the protective glycocalyx components are enzymatically degraded during angiogenesis, leading to the formation of a pannus at the lesion site and further exacerbating joint damage and cartilage destruction (*6*–*10*). Therefore, in addition to anti-inflammatory and immunomodulatory therapies, a multifaceted treatment of RA requires the combined vascular normalization to achieve a holistic therapeutic effect.

Nanomedicine represents a paradigm shift toward combinational treatment strategies. In particular, self-assembled nanostructures that form via supramolecular interactions between drug molecules exhibit excellent biocompatibility and high drug-loading capacity (*11*). Metformin (MET), a common antidiabetic drug, also notably inhibits the expression of major histocompatibility complex class II (MHC-II) and costimulatory factors, such as CD54, CD80, and CD86 (*12*, *13*), making it a promising candidate for blocking autoantigens presentation, thereby addressing the dysregulation of the immune system in RA (*14*–*18*). Given its abundant nitrogen content, MET has the capacity to form self-assembled nanostructures through hydrogen bonding with oxygen-rich TPL. However, it remains a formidable challenge to achieve effective accumulation of nanomedicines in the lesion site via the bloodstream (*19*). In the inflammatory microenvironment of RA, blood vessels exhibit hyperplasia and dilation leading to extravasation through leaky vasculature and subsequent inflammatory cell–mediated sequestration (ELVIS) effect, which allows nanodrugs to enter the joint cavity easily. However, the congestion, increased synovial fluid, and altered lymphatic flow within inflamed joints facilitate the clearance of them through the compromised vasculature (*20*, *21*). In oncology, antiangiogenic therapies aimed to vasculature normalization have proven effective in enhancing the retention of nanomedicines within tumors (*22*, *23*). Nevertheless, pharmacological interventions often have delayed and subtle effects. Endothelial cells are the main components of the vascular structure, and traditional vascular modulation approaches predominantly concentrate on the regulation of endothelial cells. Given the critical role of physical barriers such as the glycocalyx, pericytes, and basement membrane on vascular endothelium for vascular health, creating artificial physical barriers on damaged vessels may be a more effective method (*10*, *24*). A peptide sequence, SKDEEWHKNNFPLSP (STP), can efficiently bind to vascular endothelial growth factor receptor 2 (VEGFR2)–overexpressing inflamed vasculature and exhibit acid-responsive shape transformation from a random coil structure to an α-helical nanofiber (NF) network (*25*, *26*). The NF network functions as an immediate physical barrier that simultaneously addresses two critical challenges: (i) preventing intravascular nanodrug leakage to maintain therapeutic efficacy in targeting joint pathogenic cells and (ii) compensating for angiogenesis-induced glycocalyx loss to inhibit inflammatory cell infiltration into the joint cavity (*27*–*29*). In the long term, it also exerts a pharmacological intervention by inhibiting angiogenesis and restoring the normal morphology of blood vessels (*29*, *30*). The incorporation of STP into MET and TPL self-assembled nanostructures, therefore, may represent a multifunctional strategy to enhances therapeutic efficacy in RA treatment.

Meanwhile, the precise delivery of drugs to distinct targeting sites still encounters numerous obstacles. Specifically, STP must be anchored

[1]State Key Laboratory of Southwestern Chinese Medicine Resources, College of Pharmacy, Chengdu University of Traditional Chinese Medicine, Chengdu 611137, China. [2]Key Laboratory of Drug-Targeting and Drug Delivery System of the Education Ministry, West China School of Pharmacy, Sichuan University, Chengdu 610041, China. [3]Macao Centre for Research and Development in Chinese Medicine, State Key Laboratory of Quality Research in Chinese Medicine, Institute of Chinese Medical Sciences, University of Macau, Macao SAR 999078, China.
*Corresponding author. Email: cdutcmzjm@126.com (J.Z.); gaohuile@scu.edu.cn (H.G.)
†These authors contributed equally to this work.

on the vascular endothelium, whereas TPL and MET need to penetrate the deeper joint cavity and endocytosis by the abnormal cells within the lesion. Fortunately, microenvironment-responsive nanoparticles (NPs) may be a potential solution to address the challenges associated with nonspecific distribution in multiple spatiotemporal therapies for RA (*31*, *32*). As RA progresses, matrix metalloproteinase-2 (MMP2) is prominently secreted at arthritis lesions (*33*, *34*). Meanwhile, integrin $\alpha_v\beta_3$ is overexpressed on activated macrophages (MØs), osteoclasts (OCs), and fibroblast-like synoviocytes (FLSs) within the inflamed joints (*35*). Nanomedicines modified with RGD sequence notably facilitate targeted intracellular drug delivery to integrin $\alpha_v\beta_3$–positive cells (*35*, *36*). With this basis, the STP peptide was innovatively linked to the RGD peptide using an MMP2-specific cleavage peptide (GPLGV), imparting a cascade-targeting capability, abbreviated as S_R. Following MMP2 cleavage, STP-GPLG sequence separates and binds to vascular endothelium, while the VRGD mediates the specific uptake of MET and TPL self-assembled NPs (R@TM NPs) by activated MØs, OCs, and FLSs. Notably, MMP2 triggers the exposure of MET, which contains two guanidine groups and carries a positive charge under physiological conditions. This aids in resolving the charge dilemma between prolonged circulation and deep tissue penetration in RA-targeted therapies without the need for any additional chemical modifications (*37*–*39*).

In this study, we leverage the physicochemical properties of codelivered drugs and their responsiveness to the target microenvironment and construct S_R-modified TPL and MET self-assembled NPs, termed (S_R)@TM, specifically tailored for multi-spatiotemporal remodeling therapy in RA (*40*). Our approach unfolds in a series of well-orchestrated steps in vivo. (S_R)@TM specifically accumulated at RA lesions via the ELVIS effect and high binding affinity to VEGFR2, which is overexpressed by the vascular endothelial cells of inflamed arthritic joints. Excess MMP2 triggered the separation of (S_R)@TM into two parts: (i) STP-GPLG sequence forms NFs in the acidic lesion and (ii) positively charged, RGD-exposed MET- and TPL-coassembled NPs (R@TM NPs). The NFs anchored to vascular endothelium conferred triple therapeutic benefits by notably enhancing R@TM NPs retention while effectively preventing inflammatory cell recruitment and potently suppressing pathological angiogenesis. R@TM NPs showed a positive charge after the exposure of MET, enabling them to penetrate deeper into the inflamed joint. Subsequently, R@TM NPs were specifically endocytosed by activated MØs, OCs, and FLSs under the mediation of exposed RGD. The released MET inhibited T cell activation by decreasing MHC-II expression levels in antigen-presenting cells. Furthermore, it exerted synergistic effects with TPL in combating RA, including regulating the polarization of MØs, affecting the differentiation and function of OCs, and inhibiting the proliferation of synoviocytes (Fig. 1). Thus, (S_R)@TM effectively enhanced drug retention and penetration at RA lesion sites, realizing precise multiple spatiotemporal remodeling of RA. This study uses an intelligent yet straightforward carrier-free NP, offering an advanced therapeutic strategy for RA.

RESULTS

Preparation and characterization of (S_R)@TM

First, we conducted molecular docking simulations, which predicted that TPL and MET could spontaneously bind to form self-assembled nanostructures. The self-assembly mechanism is linked to the noncovalent interactions of hydrogen bonds between components (Fig. 1). We then tested three peptides with different levels of responsiveness and targeting properties to illustrate the advantages of multifunctional composite peptides. The peptide S_R (SKDEEWHKNNFPLSP-GPLG_VRGDC, where "_" denotes the MMP2 cleavage site) exhibits high affinity for VEGFR2, effectively inhibiting angiogenesis (fig. S1), and is specifically cleavable by MMP2. The resulting SKDEEWHKNNFPLSP-GPLG (STP-GPLG) sequence can self-assemble into nanofibers (NFs) under acidic conditions, while the -VRGD sequence can further target cells that overexpress integrin $\alpha_v\beta_3$. Peptide Sc_R (LIDHEWKENYFPLSF-GPLG_VRGDC, where "c" denotes "control") and peptide S (SKDEEWHKNNFPLSP-GPLG_VC) both exhibit high affinity for VEGFR2, effectively inhibit angiogenesis, and are specifically cleavable by MMP2. The key difference between these peptides is that peptide Sc_R is unable to form NFs under acidic conditions, whereas peptide S lacks the integrin $\alpha_v\beta_3$–targeting sequence (*41*). Peptides S_R, Sc_R, and S were conjugated to 1,2-Distearoyl-sn-glycero-3-phosphoethanolamine-poly(ethylene glycol)-2000-maleimide (DSPE-PEG_{2000}-MAL) via Michael addition. Successful synthesis was confirmed using matrix-assisted laser desorption/ionization-time-of-flight mass spectrometry (MALDI-TOF-MS), with peaks at mass/charge ratio (*m*/*z*) 5465 for S_R-PEG_{2000}-DSPE, *m*/*z* 5575 for Sc_R-PEG_{2000}-DSPE, and *m*/*z* 5293 for S-PEG_{2000}-DSPE (fig. S2A). Self-assembled NPs [named (S_R)@TM)] were obtained through ultrasonic emulsification combining TPL, MET, and S_R-PEG_{2000}-DPSE. (S_R)@TM exhibited a hydrated particle size of ~54 nm and spherical morphology under transmission electron microscopy (TEM). Similarly, (Sc_R)@TM and S@TM showed comparable particle sizes with narrow distributions (fig. S2B). The size and shape of (S_R)@TM were beneficial for inflamed joint accumulation through the ELVIS effect. Meanwhile, (S_R)@TM was maintained in a stable state within 24 hours in phosphate-buffered saline (PBS) containing 10% fetal bovine serum (FBS; fig. S3), indicating that (S_R)@TM is suitable for systemic administration (*42*, *43*).

Responsiveness of (S_R)@TM to MMP2 and pH

Bioinformatics analysis revealed that the genes encoding MMP2 and VEGFR2 are up-regulated in RA (fig. S4). Upon accumulation at RA lesions, (S_R)@TM undergoes a conformational change under high MMP2 concentration and acidic microenvironment conditions (*44*–*48*), triggering the separation of NFs monomers (peptide STP-GPLG sequence) and -VRGD-modified and positively charged R@TM NPs (Fig. 2A). As expected, incubation in acidic conditions in the presence of MMP2 strikingly increased the hydrated particle size and polydispersity index (PDI) value of (S_R)@TM, possibly due to NFs formation (Fig. 2B). TEM confirmed the presence of NFs with a diameter of ~14.0 nm that were composed of clusters of smaller fibers (~2.5-nm diameter) (Fig. 2C and fig. S5). MMP2 alone slightly reduced the hydrated particle size of (S_R)@TM, indicating the detachment of the STP-GPLG sequence (Fig. 2B), as corroborated by TEM results (Fig. 2C). Additionally, circular dichroism (CD) spectra showed that (S_R)@TM had a characteristic double-negative peak near 222 and 208 nm, along with a positive peak near 190 nm, indicating the formation of an α helix structure (Fig. 2D). Furthermore, (S_R)@TM exhibited a negative charge (-25.68 ± 0.77 mV) at pH 7.4, aiding in prolonged circulation. (S_R)@TM acquired a positive charge at pH 5.8 (0.93 ± 0.43 mV) and showed marked potential reversal (10.73 ± 0.57 mV) in the presence of MMP2, which was attributed to the exposure of positively charged MET (Fig. 2E).

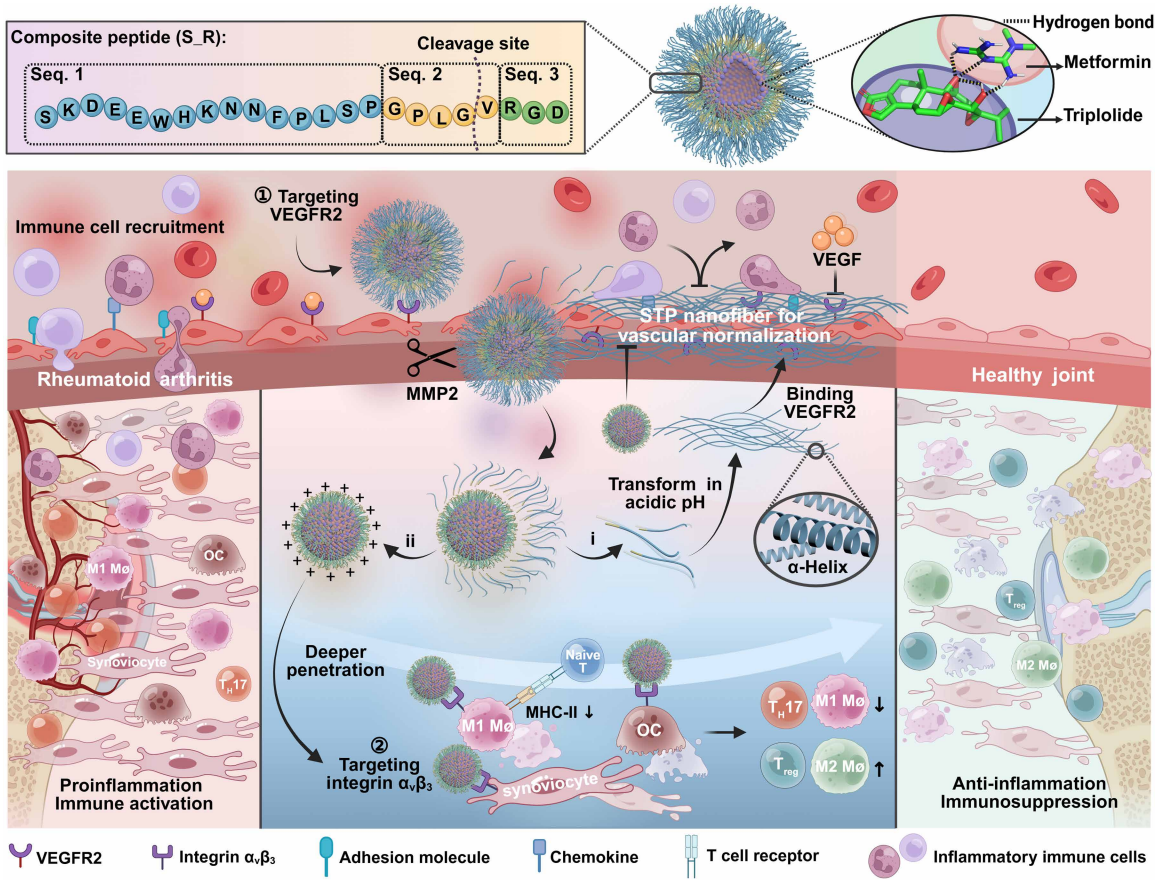

Fig. 1. Schematic illustration of (S_R)@TM preparation and therapeutic mechanism. (S_R)@TM effectively targets the inflamed vascular endothelium in rheumatoid arthritis (RA), and, upon entering the joint cavity, it is degraded by MMP2 into two parts. The peptide sequences self-assemble into STP nanofiber that bind to VEGFR2 on vascular endothelium, forming a protective nanofiber blanket. The remaining NPs (R@TM NPs) undergo charge reversal to become positively charged and expose RGD sequence, facilitating precise drug release within the joint. (S_R)@TM has different spatial distributions for multiple purposes, mediated by nanofibers and R@TM NPs. Created in BioRender. Ma, J. (2025) https://BioRender.com/xp1vn3g.

The sequentially responsive charge-reversal ability of (S_R)@TM in the presence of MMP2 and an acidic environment is imperative for drug retention and cellular uptake in the inflamed joint.

To verify the responsive release of the STP-GPLG sequence, we incubated (S_R)@TM in the presence or absence of MMP2. The results indicated that the STP-GPLG sequence is gradually released under the action of MMP2, and changes in pH do not affect its release. These results indicate that the S_R fragment exhibits MMP2-responsive cleavage, and, notably, the pH-dependent α helix transformation of STP maintains MMP2 accessibility for proteolytic cleavage without steric hindrance (Fig. 2F). Furthermore, self-assembly did not alter TPL/MET release kinetics (fig. S6). MALDI-TOF-MS analysis confirmed peptide sequence cleavage under conditions of excess MMP2, as shown in Fig. 2G, where blue arrows represent the detached STP-GPLG sequence (m/z ~2152) and green arrows represent the VRGD-PEG$_{2000}$-DSPE component (m/z ~3313). An increased number of NFs on human umbilical vein endothelial cell (HUVEC) surfaces were observed after treatment with (S_R)@TM under acidic conditions in the presence of MMP2 for 12 hours (Fig. 2H). To further demonstrate peptide detachment, we labeled S_R and Sc_R with fluorescein isothiocyanate (FITC) to prepare (S_R)$_{FITC}$ and (Sc_R)$_{FITC}$ and incorporated Rhodamine B (Rh B) to form the self-assembled nanostructures, prepared (S_R)$_{FITC}$@TM$_{Rh\ B}$ and (Sc_R)$_{FITC}$@TM$_{Rh\ B}$, and applied them to HUVECs, using fluorescence resonance energy transfer (FRET) effect to investigate their detachment. In the absence of MMP2 treatment, both (S_R)$_{FITC}$@TM$_{Rh\ B}$ and (Sc_R)$_{FITC}$@TM$_{Rh\ B}$ groups exhibited Rh B intensity under FITC excitation due to the FRET effect. MMP2 incubation resulted in the cleavage of (S_R)$_{FITC}$ and an increase in the spatial distance between FITC-labeled NFs monomers and Rh B–encapsulated TM$_{Rh\ B}$ NPs, thus disrupting the FRET effects. FITC fluorescence was observed postincubation, while Rh B fluorescence was absent (Fig. 2I). The findings reveal that (S_R)@TM can be efficiently cleaved by MMP2, with the released STP-GPLG sequence subsequently self-assembling into NFs under acidic conditions, thereby exhibiting the potential to form an NFs network around inflamed joints.

In vitro spatiotemporal targeting and distribution analysis

First, we labeled the peptide with FITC and incorporated 1,1′-dioctadecyl-3,3,3′,3′-tetramethylindodicarbocyanine (DiD) to prepare (S_R)$_{FITC}$@TM$_{DiD}$ and (Sc_R)$_{FITC}$@TM$_{DiD}$ to investigate the VEGFR2 targeting specificity of (S_R)@TM and the vascular anchoring of STP. Under tumor necrosis factor–α (TNF-α)–induced inflammatory conditions, HUVECs exhibit higher expression of VEGFR2

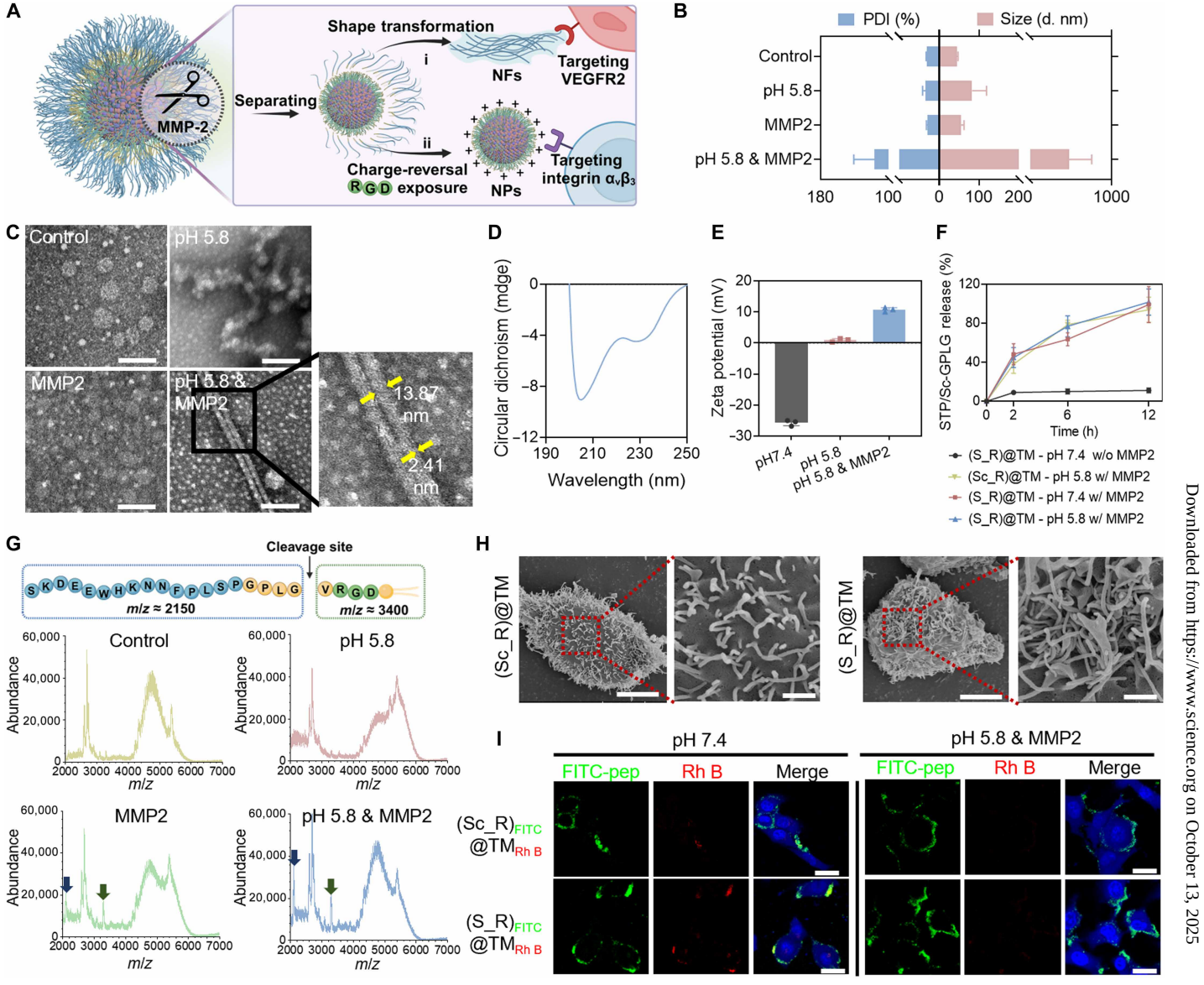

Fig. 2. Sequentially responsiveness of (S_R)@TM to MMP2 and pH. (**A**) Schematic illustration of the dual response of (S_R)@TM to MMP2 and pH, manifested by the detachment of STP-GPLG and its shape transform into NFs, while the remaining R@TM NPs undergo a charge reversal from negative to positive, exposing the RGD motif. Created in BioRender. Ma, J. (2025) https://BioRender.com/0h1mhv6. (**B**) Diameter (d. nm) and PDI value of (S_R)@TM under different conditions ($n = 3$ independent samples). (**C**) Transmission electron microscopy (TEM) images of (S_R)@TM after incubation under different conditions. Scale bars, 100 μm. (**D**) Circular dichroism spectra of (S_R)@TM under acidic conditions in the presence of MMP2. The y-axis represents ellipticity in millidegrees (mdeg). (**E**) Zeta potential of (S_R)@TM under different conditions ($n = 3$ independent samples). (**F**) The release of the STP-GPLG sequence from (S_R)@TM and Sc-GPLG from (Sc_R)@TM under various conditions ($n = 3$ independent samples). w/, with; w/o, without; h, hours. (**G**) Schematic illustration of S_R-PEG_{2000}-DSPE cleavage. Matrix-assisted laser desorption/ionization-time-of-flight mass spectrometry (MALDI-TOF-MS) analyses of (S_R)@TM postincubation, showing STP-GPLG sequence (blue arrows) and remaining fragments (green arrows). (**H**) Representative scanning electron microscopy (SEM) images of HUVECs incubated with (S_R)@TM under acidic conditions in the presence of MMP2. Scale bars, (left) 5 μm and (right) 1 μm. (**I**) The fluorescence resonance energy transfer (FRET) effect of $(Sc\_R)_{FITC}@TM_{Rh\ B}$ and $(S\_R)_{FITC}@TM_{Rh\ B}$, with or without MMP2 response, was verified using confocal laser scanning microscopy (CLSM). Scale bars, 20 μm. Data in [(B), (E), and (F)] were presented as means ± SD.

(fig. S7A) (*49*). L929 cells, which do not express VEGFR2, demonstrated minimal uptake of $(S\_R)_{FITC}@TM_{DiD}$. In contrast, HUVECs exhibited notably increased green and red fluorescence signals, particularly under TNF-α–induced inflammatory conditions. The enhanced fluorescence strongly indicated the good VEGFR2-targeting capability of $(Sc\_R)_{FITC}@TM_{DiD}$ and $(S\_R)_{FITC}@TM_{DiD}$. In the MMP2-pretreated group, reduced red fluorescence indicated decreased uptake, which is likely attributed to STP-GPLG cleavage leading to reduced VEGFR2 targeting. However, substantial green fluorescence was observed on the cell membrane, indicating that the cleaved STP-GPLG sequence is anchored to the cellular membrane (Fig. 3A and fig. S8). These findings were corroborated by flow cytometry (FCM) results (Fig. 3, B and C). Furthermore, transwell assays were used to mimic an in vitro inflammatory vascular model (Fig. 3D). After incubation

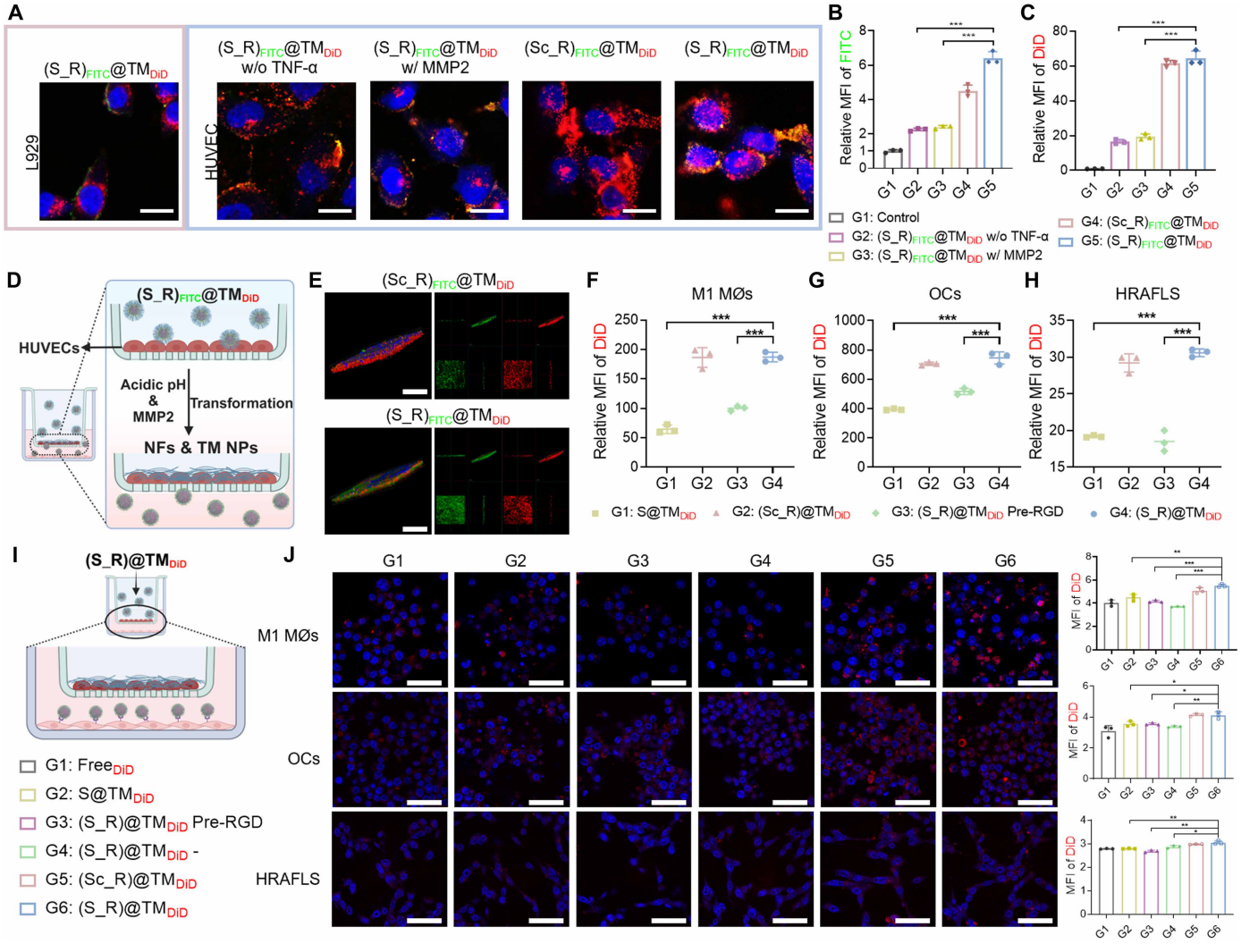

Fig. 3. In vitro spatiotemporal targeting and distribution analysis. (**A**) Fluorescence images of HUVECs after treatment with (Sc_R)/$(S_R)_{FITC}$@TM_{DiD} for 3 hours. Scale bars, 20 μm. Flow cytometry (FCM) analysis of (**B**) FITC and (**C**) DiD in HUVECs after 3 hours of different treatments ($n = 3$ biologically independent cell samples). In (A) to (C), "w/o TNF-α" indicates cells without TNF-α treatment, and "w/ MMP2" indicates that (S_R)@TM with MMP2 treatment. (**D**) Schematic illustration of (S_R)@TM penetrating vascular model simulated and NFs anchoring to vascular endothelium in vitro using a transwell apparatus. Created in BioRender. Ma, J. (2025) https://BioRender.com/hdr4vjh. (**E**) Three-dimensional fluorescence images of $(Sc_R)_{FITC}$@TM_{DiD} and $(S_R)_{FITC}$@TM_{DiD} in vascular models for 3 hours. Scale bars, 200 μm. FCM detection of DiD uptake by M1 MØs (**F**), OCs (**G**), and human RA FLS (HRAFLSs) (**H**) after different treatments ($n = 3$ biologically independent cell samples). (**I**) Schematic illustration of in vitro simulation of (S_R)@TM penetration through vascular endothelium and $\alpha_v\beta_3$-targeting by detached R@TM_{DiD} NPs. Created in BioRender. Ma, J. (2025) https://BioRender.com/ghfx3x7. (**J**) Confocal microscopy images of DiD fluorescence in M1 MØs, OCs, and HRAFLSs after treatment with different formulations from (I). Scale bars, 50 μm. Semiquantitative analysis of DiD fluorescence intensity is shown on the right side ($n = 3$ biologically independent cell samples). G4 refers to (S_R)@TM without MMP2 treatment. Data in [(B), (C), (F), (G), (H), and (J)] were presented as means ± SD. *P* values were determined by two-sided Student's *t* test. $^*P < 0.05$; $^{**}P < 0.01$; $^{***}P < 0.001$.

with $(Sc_R)_{FITC}$@TM_{DiD} or $(S_R)_{FITC}$@TM_{DiD}, three-dimensional confocal laser scanning microscopy (CLSM) of the transwell cell layer revealed that (S_R)@TM demonstrated significantly stronger FITC fluorescence signals compared to (Sc_R)@TM (1.24-fold increase in fluorescence intensity, $P < 0.05$) (Fig. 3E and fig. S9). Additionally, FITC-labeled NFs of (S_R)@TM were uniformly distributed throughout the entire thickness of HUVEC layers, with a fluorescence intensity ratio of 1.51 ± 0.11 between the basal and luminal of the cell layer. These findings indicate that (S_R)@TM, through STP mediation, selectively accumulates on VEGFR2-high vascular endothelium. Upon exposure to MMP2, the STP-GPLG sequence undergoes degradation, transforming into NF structures that anchor to endothelial cells. Consequently, the NFs network exhibits prolonged retention on the vascular endothelium, effectively functioning as an NF blanket to restore endothelial barrier function.

Subsequently, we verified the integrin $\alpha_v\beta_3$–targeting ability of VRGD-modified R@TM_{DiD} NPs. RAW 264.7 cells can be differentiated into M1 MØs by lipopolysaccharide (LPS) stimulation and into OCs by RANKL stimulation. The expression of $\alpha_v\beta_3$ was found to increase by 1.75-fold and 2.41-fold (both $P < 0.001$), respectively, following these differentiation processes (fig. S7, B and C). FCM analysis confirmed that (S_R)@TM had excellent targeting ability

toward M1 MØs, OCs, and human RA FLSs (HRAFLSs) in an MMP2-overexpressing environment. Reduced uptake in the RGD-preblocked group and the S@TM_{DiD} group suggested that (S_R)@TM_{DiD} was internalized via RGD-mediated mechanisms (Fig. 3, F to H). To mimic the arthritis microenvironment, an in vitro transwell vascular model was used to simulate the capillary barrier in the joint. Given the abundant presence of M1 MØs, OCs, and FLSs within the inflamed joint cavity (*18*), we seeded M1 MØs, OCs, and HRAFLSs in the lower chamber of a transwell apparatus (Fig. 3I). After different treatments, similar DiD fluorescence intensities of the cell layer indicated that the modification with different functional composite peptides (S_R, Sc_R, and S) had no effect on the ability of the nanostructures to penetrate vascular endothelium (fig. S10). CLSM imaging of the lower transwell chamber indicated decreased cellular uptake of (S_R)@TM after RGD blocking (group G3), and S@TM_{DiD} and non-MMP2 (S_R)@TM_{DiD} (group G4) showed less cellular uptake than (S_R)@TM, indicating that the uptake of R@TM_{DiD} NPs by these cells relies on RGD mediation. Meanwhile, (Sc_R)@TM_{DiD} showed slightly lower uptake levels than (S_R)@TM_{DiD}, possibly due to the physical barrier effect of NFs, which reduced the leakage of R@TM_{DiD} NPs (Fig. 3J). These findings highlighted the robust VEGFR2 and integrin $\alpha_v\beta_3$ cascade–targeting capabilities of (S_R)@TM driven by the specific inflammatory joint microenvironment. Encouragingly, we have found that NFs enhance the intracellular internalization of R@TM_{DiD} NPs by reducing their leakage.

In vitro multiple spatiotemporal anti-RA effects

As RA progresses, the enzymatic degradation of the protective glycocalyx components leads to the continuous recruitment of inflammatory cells to inflammation sites via blood capillaries (*16*, *50*). To verify that (S_R)@TM reduced the recruitment of inflammatory cells, 5-chloromethylfluorescein-diacetate (CMFDA)–labeled human monocytic leukemia THP-1 cells were incubated with an established in vitro vascular model to mimic the process of inflammatory immune cell recruitment (Fig. 4A). As expected, after 3 hours of incubation, the groups lacking NFs [(Sc_R)@TM] and nonacidic group [(S_R)@TM-] displayed comparable limitations in inhibiting THP-1 cell adhesion, similar to the control group, while S@TM and (S_R)@TM groups (containing STP NFs) demonstrating significantly reduced THP-1 cell adhesion (2.02- and 2.06-fold lower, respectively, both $P < 0.01$) compared to the non–fiber-forming (Sc_R)@TM group. The (S_R)@TM demonstrated significantly enhanced efficacy under acidic conditions, exhibiting a 2.39-fold reduction ($P < 0.01$) in suppressing THP-1 cell adhesion compared to (S_R)@TM without MMP2 and under nonacidic conditions [(S_R)@TM-], consistent with its pH-dependent fiber formation mechanism (Fig. 4B). This finding underscores the robust short-term physical barrier function of STP NFs formed on inflamed vascular endothelium in suppressing inflammatory cell recruitment. Based on the modulation of inflammatory cytokine secretion by HRAFLSs in the lower chamber through R@TM NPs, which may indirectly regulate the morphology of endothelial cells, we prolonged the incubation time to 12 hours to evaluate the synergistic spatiotemporal remodeling effect on inflammatory cell migration. The number of THP-1 cells in each formulation group was less at 12 hours than at 3 hours, especially for the (S_R)@TM group, in which the number was 20 times less than at 3 hours, indicating that the STP NFs not only provide a rapid reduction in inflammatory cell adhesion in the short term but also work in concert with R@TM NPs to repair the function of vascular endothelial cells for long-term effects (Fig. 4C). The VEGFR2-binding STP and the resulting NF formation contributed to the inhibition of angiogenesis. Subsequently, we investigated the angiogenesis-inhibiting ability of (S_R)@TM in HUVECs. The tubular nodule formation assay demonstrated significantly higher nodule counts in the (Sc_R)@TM group compared to the (S_R)@TM group, with 2.27-fold ($P < 0.01$) and 1.89-fold ($P < 0.05$) increases observed at 6 and 10 hours posttreatment, respectively (Fig. 4D and fig. S11). These results indicate that the NFs detached from (S_R)@TM notably inhibit angiogenesis.

The presentation of antigens to T cells by MHC-II on APCs is enhanced, and the activation of plasma cells within the joint to produce autoantibodies is associated with the progression of RA (*16*). FCM results indicated that MET alone reduced the effect by 2.27 times ($P < 0.01$). Furthermore, the groups treated with S@TM, (Sc_R)@TM, and (S_R)@TM exhibited 1.18, 1.18, and 1.39 times lower MHC-II expression compared to the free MET group, respectively (Fig. 4E). These results suggested that the application of MET leads to a reduction in MHC-II expression, potentially reducing activation effect on helper T cell. Furthermore, FCM analysis confirmed that (S_R)@TM prevented MØ polarization toward the M1 phenotype (fig. S12). TPL exhibited significant cytotoxicity toward M1 MØs, OCs, and HRAFLSs. The coadministration of TPL and MET did not alter the cytotoxic profile of TPL. Furthermore, the cytotoxic effects persisted following NP preparation (Fig. 4, F to H, and figs. S13 and S14). In addition, both TPL and MET inhibited OC differentiation. However, the number of OCs was least in the (S_R)@TM groups (fig. S15A). Similarly, TPL and MET inhibited bone resorption, with notable decreases in bone resorption pits observed in the (S_R)@TM- and (Sc_R)@TM-treated groups compared with the control group (fig. S15B). These findings indicated that (S_R)@TM remarkably alleviated RA through multiple spatiotemporal remodeling steps, encompassing inhibiting inflammatory cell recruitment and angiogenesis, down-regulating MHC-II expression, inhibiting pro-inflammatory MØ polarization, modulating OCs functions, and suppressing synoviocytes proliferation by R@TM NPs.

Encouraged by the excellent dual-responsive cascade-targeting and multiple spatiotemporal anti-RA effects in vitro, we further investigated the targeting and retention abilities of (S_R)@TM_{DiD} in a rat model of antigen-induced arthritis (AIA) (Fig. 5A). Representative micro–computed tomography (CT) images of the ankle joints revealed the successful establishment of the AIA model (fig. S16). Additionally, the increased levels of MMP2, VEGFR2, and $\alpha_v\beta_3$ in the joints of AIA model rats compared to healthy rats further validate the successful establishment of the AIA model and its suitability for evaluating the efficacy of our nanosystem (fig. S17). DiD fluorescence in all groups peaked at 24 hours. Although S@TM_{DiD} targeted vascular endothelium at the lesion site, the amount of DiD accumulation at the joint was lower than (S_R)@TM_{DiD} group may be because of the lack of the RGD. Both the (Sc_R)@TM_{DiD} and (S_R)@TM_{DiD} groups effectively targeted the joint. However, in the (Sc_R)@TM_{DiD} group, the fluorescence gradually decreased after 24 hours. In contrast, substantial DiD fluorescence persisted at the joint site at 48 hours in the (S_R)@TM_{DiD} groups. This was attributed to NF formation, which enhancing drug retention in inflamed joints (Fig. 5B). Ex vivo fluorescence analysis revealed that the fluorescence intensity in joints treated with S@TM_{DiD}, (Sc_R)@TM_{DiD}, and (S_R)@TM_{DiD} was 2.42, 3.10, and 6.54 times higher in joints than in those treated with free DiD ($P < 0.001$), respectively, indicating

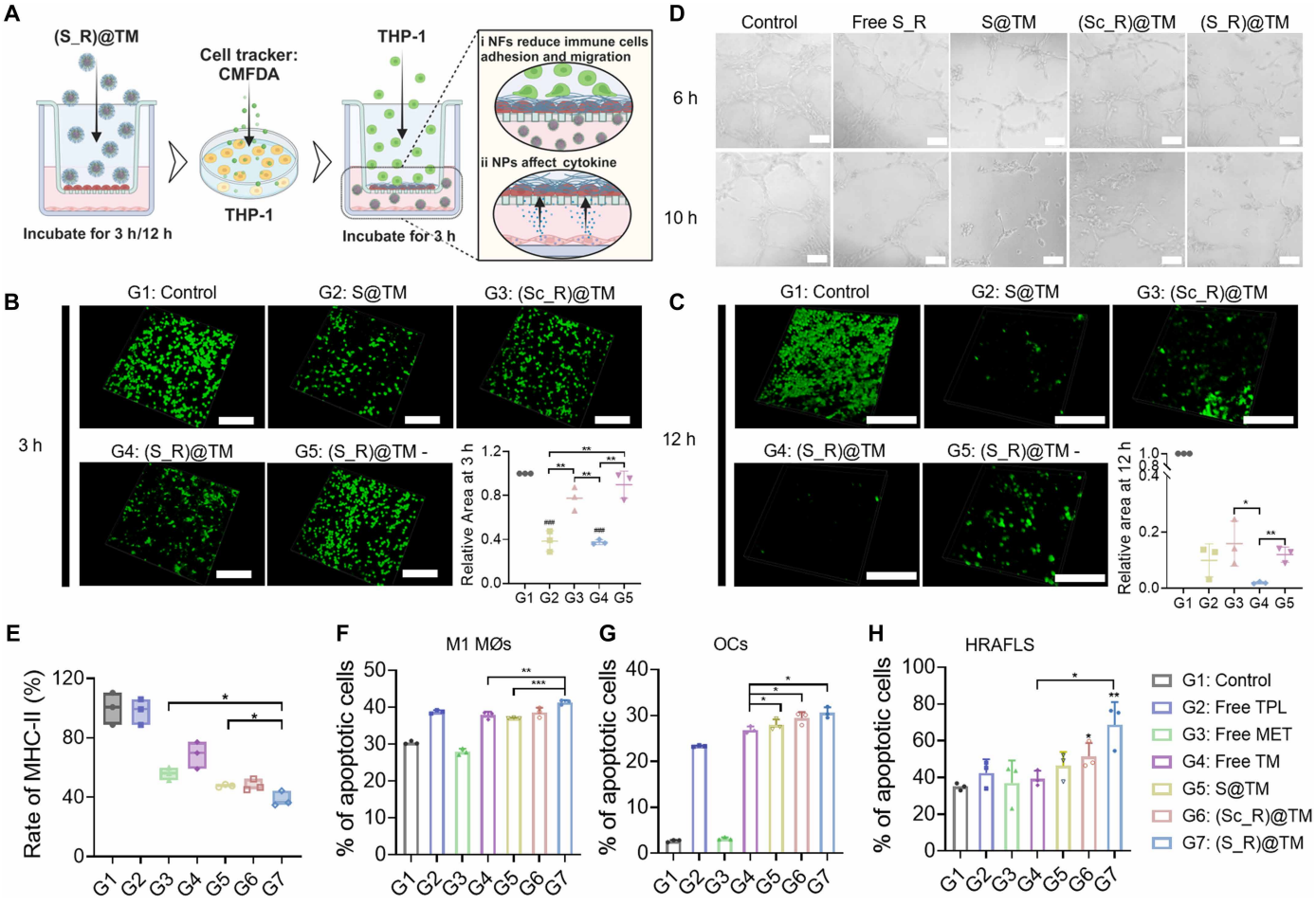

Fig. 4. In vitro multiple spatiotemporal anti-RA effects. (**A**) Schematic illustration in vitro simulation of NFs forming a physical barrier to directly inhibit inflammatory cell recruitment in the short term and indirectly inhibit inflammatory cell recruitment by regulating blood vessels and the microenvironment in the long term. Created in BioRender. Ma, J. (2025) https://BioRender.com/rsuvpn4. Three-dimensional fluorescence images of the in vitro vascular model after different treatments for 3 hours (**B**) and 12 hours (**C**), and coincubation with 5-chloromethylfluorescein-diacetate (CMFDA)–labeled THP-1 cells. Scale bars, 200 μm. Semiquantitative analysis of THP-1 cell adhesion to the vascular models using ImageJ software ($n = 3$ biologically independent cell samples). G5 in (B) and (C) denotes (S_R)@TM that neither has undergone MMP2 treatment nor has been exposed to acidic conditions. (**D**) Tubular image of HUVECs under different treatments for 6 and 10 hours. Scale bars, 100 μm. h, hours. (**E**) Reduced MHC-II levels in RAW 264.7 cells induced by LPS after different treatments ($n = 3$ biologically independent cell samples). FCM analysis of apoptosis of M1 MØs (**F**), OCs (**G**), and HRAFLSs (**H**) after different treatments ($n = 3$ biologically independent cell samples). Data in [(B), (C), and (E) to (H)] were presented as means ± SD. *P* values were determined by two-sided Student's *t* test. $^*P < 0.05$; $^{**}P < 0.01$; $^{***}P < 0.001$. In (B), ### indicates $P < 0.001$ for comparisons with the G1 group.

that the charge reversal and exposure of VRGD further reduced the leakage of R@TM_{DiD} NPs and extended its retention. Furthermore, the formulation of NFs enhanced specific inflamed ankle joints accumulation. The extended retention time at the lesion site delayed the metabolism of (S_R)@TM_{DiD}, leading to the strongest fluorescence intensity in the liver at 48 hours (Fig. 5, C to E). The abovementioned results indicated that (S_R)@TM had excellent cascade-targeting ability in vivo and that NF formation notably slowed drug leakage from joint lesions.

To elucidate the mechanism responsible for the high level of (S_R)@TM accumulation, synovium slices were stained with a neovascular marker (CD31) and a lymphatic marker (LYVE-1) (Fig. 5, F to H). The synovium in patients with RA exhibits persistent proliferation, which is dependent on neovascularization within the synovial tissue, and these capillaries exacerbate inflammatory responses and joint degradation (*51*). Colocalization between FITC-labeled peptides and CD31-labeled neovasculature was observed, indicating the effective VEGFR2 targeting efficiency of both $(Sc\_R)_{FITC}$@TM_{DiD} and $(S\_R)_{FITC}$@TM_{DiD} (Fig. 5I and fig. S18A). In contrast, R@TM_{DiD} NPs penetrated deeper tissues, mediated by their positive charge and targeting properties, which resulted in weak colocalization with CD31 (Fig. 5J and fig. S18A). Moreover, increased lymphatic angiogenesis and lymphatic flow at arthritic sites accelerates drug clearance from inflamed joints (*21*, *52*). To investigate whether NF formation affects drug leakage, we labeled lymph capillaries with anti–LYVE-1 (Fig. 5H). DiD in $(S\_R)_{FITC}$@TM_{DiD} were preferentially retained at the synovium site. However, DiD in $(Sc\_R)_{FITC}$@TM_{DiD} colocalized strongly with lymphatic vessels, indicating that R@TM_{DiD} NPs were cleared through the lymphatic system (Fig. 5K and fig. S18B). Additionally, the $(S\_R)_{FITC}$@TM_{DiD} group exhibited

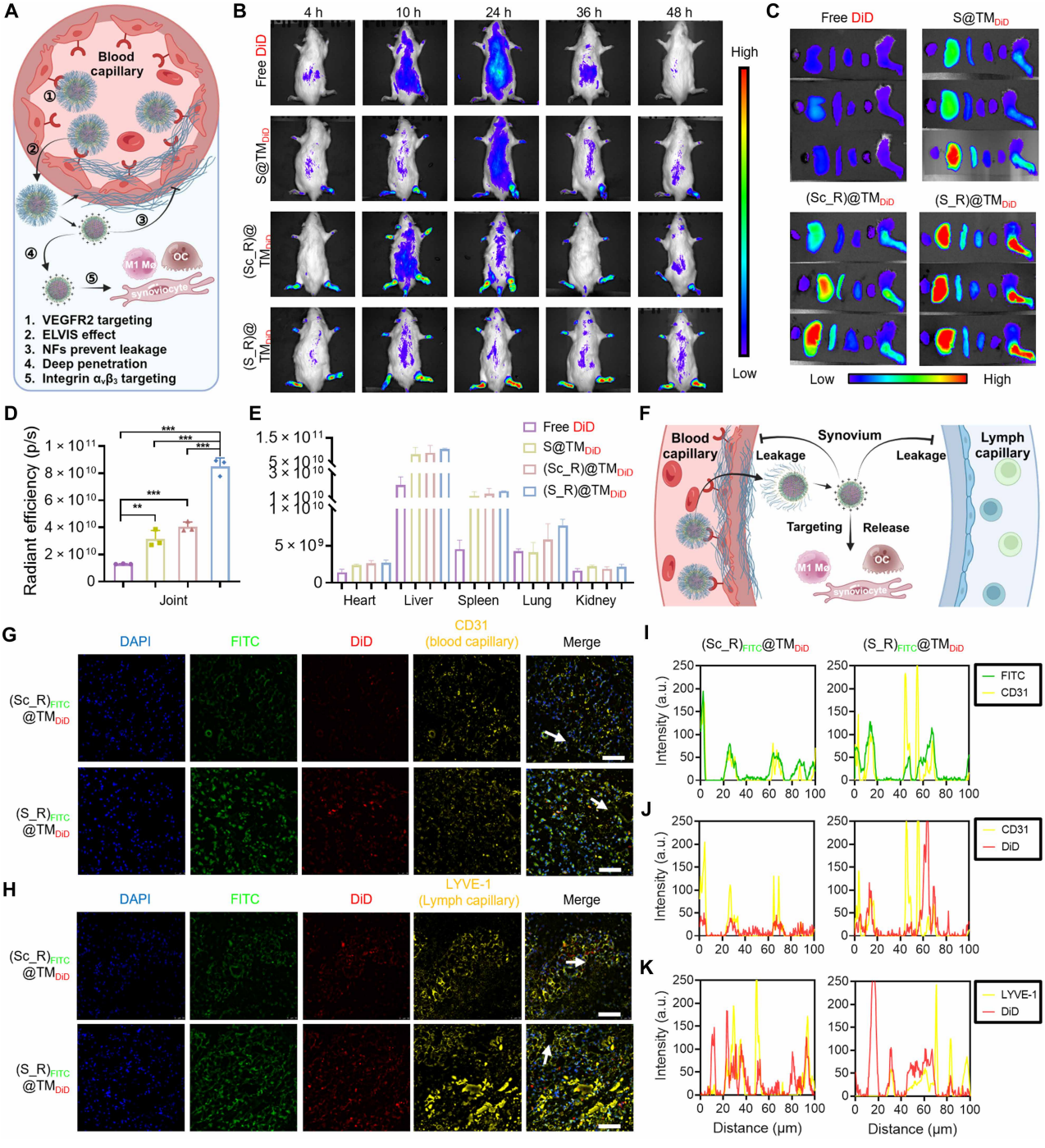

Fig. 5. Biodistribution of (S_R)@TM. (**A**) Schematic illustration of (S_R)@TM cascade-targeting to inflamed joints with long-term retention Created in BioRender. Ma, J. (2025) https://BioRender.com/64xvb4e. (**B**) In vivo fluorescence images at 4, 10, 24, 36, and 48 hours after intravenous injection of different NPs. h, hours. (**C**) Ex vivo images of major organs harvested from different treatment groups at 48 hours. From left to right is the heart, liver, spleen, lung, kidney, and inflammatory joint. Quantification of joint fluorescence (**D**) and main organ (**E**) fluorescence at 48 hours for different treatment groups ($n = 3$ biologically independent mice). (**F**) Schematic illustration of NFs and R@TM NPs in the synovium of the joints. Created in BioRender. Ma, J. (2025) https://BioRender.com/avopjve. Confocal images of different FITC-DiD formulations in synovium blood capillary (**G**) and lymph capillary (**H**) in inflamed joints. Blood capillary and lymph capillary were identified by immunofluorescence analysis of CD31 and LYVE-1 (yellow fluorescence), respectively. Scale bars, 100 μm. (**I**) Colocalization analysis of FITC and DiD fluorescence along the white arrows marked in (G). (**J**) Colocalization analysis of Cy3 (CD31) and DiD fluorescence along the white arrows marked in (G). (**K**) Colocalization analysis of Cy3 (LYVE-1) and DiD fluorescence along the white arrows marked in (H). a.u., arbitrary units. Data in [(D) and (E)] were presented as means ± SD. *P* values were determined by two-sided Student's *t* test. $^{**}P < 0.01$; $^{***}P < 0.001$.

higher FITC and DiD fluorescence than $(Sc\_R)_{FITC}@TM_{DiD}$ group, with 2.56-fold higher FITC fluorescence than $(Sc\_R)_{FITC}@TM_{DiD}$ ($P < 0.001$) (fig. S18C). The abovementioned results demonstrate that (S_R)@TM-derived NFs effectively prevent R@TM NPs leakage while enhancing vascular retention of VEGFR2-targeting peptides, with their charge-reversal capability and microenvironment-responsive cascade targeting synergistically promoting deep R@TM NP distribution in arthritic joints.

In vivo anti-RA efficiency

Last, after observing promising cellular-level therapeutic effects and distribution results, in vivo anti-RA efficiency was evaluated according to the treatment schedule outlined in Fig. 6A. Throughout the treatment period, the weight change trend in nanostructure formulation–treated rats closely resembled that of control rats, indicating no apparent toxicity for any of the formulations tested (Fig. 6B). At the end point of treatment, the free TM group exhibited reduced ulceration and swelling, with further improvement seen with S@TM. Substantial symptom reduction was observed with (Sc_R)@TM and (S_R)@TM, and the paw condition of the (S_R)@TM group approached that of the healthy control group (fig. S19). Furthermore, free TM, S@TM, and (Sc_R)@TM treatment had limited effects in terms of reducing the paw thickness, ankle diameter, and arthritis scores (Fig. 6, C to E). However, rats treated with (S_R)@TM showed a significant reduction in all measured parameters, suggesting the superior therapeutic potential of (S_R)@TM for RA.

Micro-CT images showed that, compared with the model group, bone destruction in the S@TM and (Sc_R)@TM groups was reduced by 1.88 and 2.14 times (both $P < 0.05$), respectively, while the (S_R)@TM group exhibited no significant bone erosion similar to the healthy group. In contrast, the (S_R)@TM group exhibited a 7.50 times reduction in bone destruction ($P < 0.001$), approaching levels observed in the healthy group (Fig. 6F and fig. S20). Hematoxylin and eosin (H&E) staining revealed extensive infiltration of inflammatory cells in the knee synovium of model rats, which was progressively alleviated after treatment with S@TM, (Sc_R)@TM, and (S_R)@TM (fig. S21). Additionally, the area of CD31 expression decreased by 2.69, 1.54, and 3.65 times in S@TM-, (Sc_R)@TM-, and (S_R)@TM-treated rats, respectively. In addition, the (S_R)@TM exhibited 2.37-fold reduction in vascular density than (Sc_R)@TM ($P < 0.05$), demonstrating excellent the antiangiogenesis ability of (S_R)@TM in vivo (fig. S22A). Through bio-electron microscopy, tight junctions between endothelial cells in the synovial tissues of model group rats were difficult to observe. In contrast, endothelial cells in the synovial tissues of (S_R)@TM-treated rats exhibited higher tight junction levels (indicated by yellow arrows). Clear NF structures were also observed around the blood vessels (Fig. 6G). Immunohistochemical staining for zona occludens 1 (ZO-1) and immunofluorescence detection of glycosaminoglycan-related component in synovial tissues (aggrecan) further support these findings. The model group exhibited an increase in neovascularization and reduced expression levels of ZO-1 (Fig. 6, H and I) and aggrecan (Fig. 6, J and K). Quantitative analysis revealed that STP-treated groups exhibited significantly enhanced expression of the tight junction protein ZO-1, with (S_R)@TM and S@TM showing 2.79-fold and 2.61-fold upregulation, respectively, compared to the model group (both $P < 0.01$). Notably, both formulations also demonstrated superior efficacy over (Sc_R)@TM, increasing ZO-1 levels by 1.48- to 1.57-fold (both $P < 0.05$). Moreover, (S_R)@TM displayed robust restorative effects on glycocalyx integrity, significantly elevating aggrecan compared to (Sc_R)@TM ($P < 0.05$). CD51 staining indicated increased OC differentiation in rats with AIA. Because of the notable reduction in OC differentiation capacity by TPL and MET, OC differentiation was significantly reduced in treated rats, with a 2.20 times reduction ($P < 0.01$) after (S_R)@TM treatment (fig. S22B). These findings suggest that (S_R)@TM can reduce inflammatory cell infiltration, suppress angiogenesis, and regulate vascular morphology while also effectively inhibiting OC differentiation through enhanced drug delivery efficiency and comprehensive treatment strategy.

The down-regulation of MHC-II by MET limits T cell activation. Additionally, NFs forming on the vascular endothelium, acting as a physical barrier. This reduced the recruitment of inflammatory cells (e.g., MØs, neutrophils, and monocytes) and activated T cells into the joint cavity (Fig. 7A). Immunohistochemical staining of synovium tissue sections revealed substantially increased MHC-II expression levels in AIA rats compared to healthy controls. Treatment with free TM led to a reduction in red fluorescence, attributed to the down-regulation of MHC-II by MET. A further decrease in red fluorescence was observed following treatment with different formulations (Fig. 7B). To assess the impact of (S_R)@TM on inflammatory cell recruitment, we conducted immunofluorescence staining of synovium tissue sections. Compared with healthy rats, AIA rats showed notably increased fluorescence intensity for CD86 (M1 MØs), Ly6G (neutrophils), and CD14 (monocytes), indicating sustained inflammatory cell recruitment to RA joints. After treatment with different nanostructures formulations, substantial reductions in fluorescence intensities were observed, particularly for CD86, whereas CD206 (M2 MØs) levels remained unchanged. The reduction in the M1/M2 MØ ratio suggested enhanced inhibition of inflammation. The fluorescence intensities of CD86, Ly6G, and CD14 were lower in rats treated with S@TM and (S_R)@TM than in those treated with (Sc_R)@TM, suggesting that the STP NFs formed on the vascular endothelium at the site of inflammation fully exerts its physical barrier function, effectively inhibiting the recruitment of inflammatory cells (Fig. 7C).

To further assess the effect of (S_R)@TM on T cell activation, we conducted immunofluorescence staining to detect CD3, CD4, FOXP3, and interleukin-17 (IL-17) in synovium tissue sections. After treatment with free TM, reductions in CD3 and IL-17 fluorescence intensity were observed, suggesting that free TM mitigated T cell recruitment and T helper 17 (T_H17) cell differentiation. In S@TM- and (Sc_R)@TM-treated rats, CD3 fluorescence intensity further decreased, and IL-17 fluorescence was nearly absent, indicating significant inhibition of T cell activation and differentiation toward T_H17 cells. Notably, in (S_R)@TM-treated rats, CD3 fluorescence was scarcely detectable, suggesting that the combination of NFs with targeted delivery of MET and TPL effectively coregulated T cell differentiation and reduced immune cell recruitment to the synovium tissue. The differences in FOXP3 fluorescence intensity among the groups were not statistically significant, which may be due to the inherently low recruitment of regulatory T cells (T_{reg} cells) into the joint cavity in the AIA model (Fig. 7D). These results indicate that (S_R)@TM effectively attenuated inflammatory cell recruitment and T cell activation in inflamed joints.

In vivo immunomodulatory

To evaluate immunomodulatory effects, we examined T cell subtypes in the spleens of rats (fig. S23). AIA model rats showed a

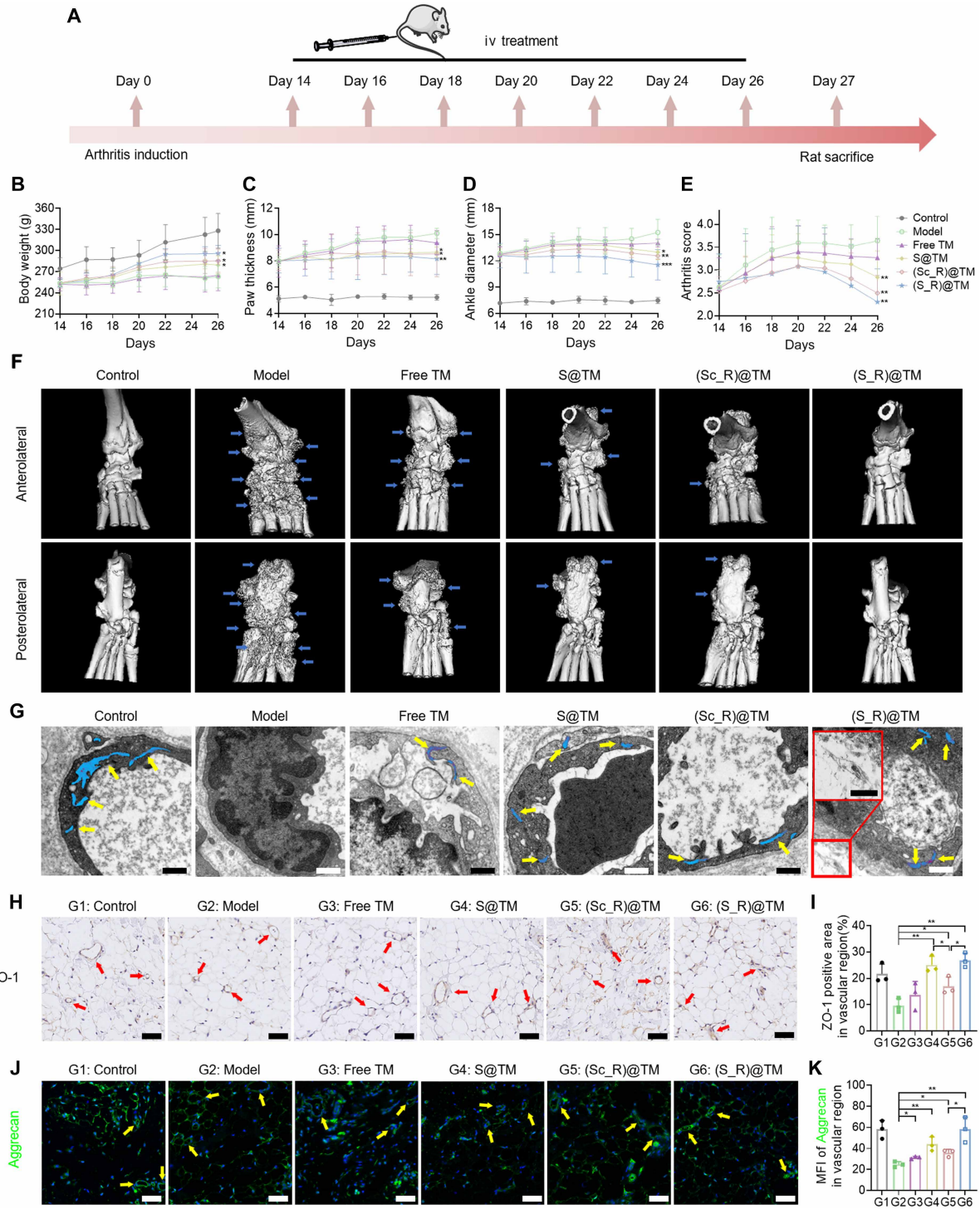

Fig. 6. In vivo anti-RA efficiency of (S_R)@TM. (**A**) Schematic illustration showing the procedures for treating rats with AIA with different treatment regimens. iv, intravenous. Body weight (**B**), paw thickness (**C**), ankle diameter (**D**), and arthritis score (**E**) of rats with AIA during the treatment period. Data represent the means ± SD ($n = 7$ biologically independent mice). (**F**) Representative micro-CT images of the ankle joints from various treatment groups at the end point of the experiment. Blue arrows indicate sites of bone erosion. (**G**) bio-TEM images of synovium tissue in rats with different treatments. Yellow arrows indicate tight junctions between endothelial cells, and red box highlights NFs. Scale bars, 500 nm; scale bar, 200 nm (after magnification). (**H**) Representative ZO-1 immunohistochemistry of synovial tissues (scale bars, 50 μm; red arrows denote vasculature). (**I**) Quantitative analysis of ZO-1$^+$ vascular area ($n = 3$ biologically independent mice). (**J**) Aggrecan immunofluorescence in synovium (scale bars, 50 μm; yellow arrows indicate vessels). (**K**) Quantitative analysis of aggrecan mean fluorescence intensity (MFI) in synovium ($n = 3$ biologically independent mice). Data in [(B) to (E), (I), and (K)] were presented as means ± SD. *P* values were determined by two-sided Student's *t* test. $^*P < 0.05$; $^{**}P < 0.01$; $^{***}P < 0.001$.

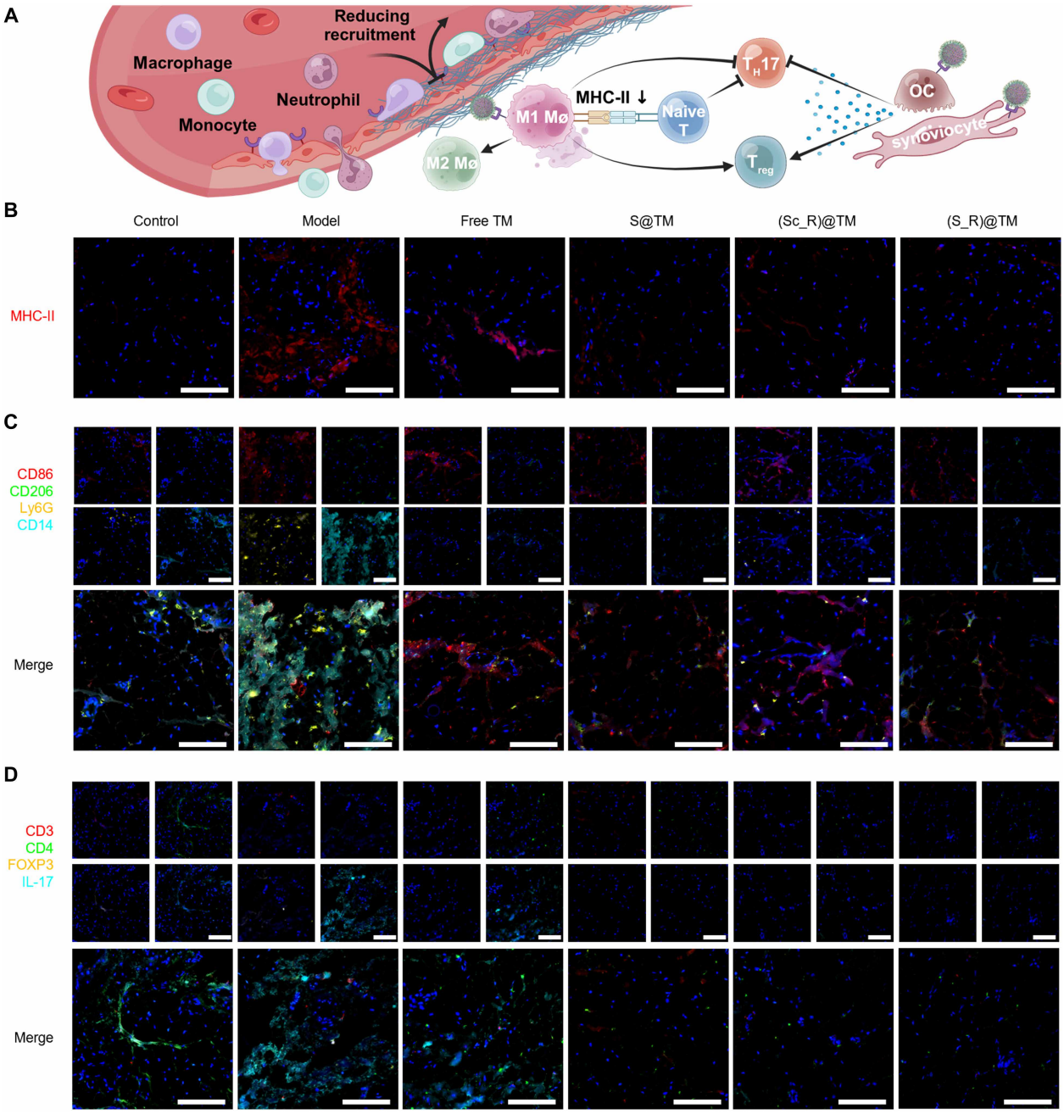

Fig. 7. Inflammatory cell recruitment and immune cell activation analysis. (**A**) Schematic illustration of the anti-RA mechanism of (S_R)@TM. Created in BioRender. Ma, J. (2025) https://BioRender.com/mibwbna. (**B**) Representative fluorescence images of synovium tissue sections stained with anti-MHC-II (red). Blue indicates 4′,6-diamidino-2-phenylindole (DAPI) (scale bars, 100 μm). (**C**) Representative fluorescence images of synovium tissue sections stained with anti-CD86 (red), anti-CD206 (green), anti-Ly6G (yellow), and anti-CD14 (cyan). Blue indicates DAPI (scale bars, 100 μm). (**D**) Representative fluorescence images of synovium tissue sections stained with anti-CD3 (red), anti-CD4 (green), anti-FOXP3 (yellow), and anti-IL-17 (cyan). Blue indicates DAPI (scale bars, 100 μm).

decrease in the total T cell count. Free TM partially restored the T cell count, while NP treatment further attenuated the reduction. Notably, (S_R)@TM exhibited T cell counts surpassing those of healthy rats (Fig. 8, A and B). $CD4^+$ T cell numbers were markedly elevated in rats with AIA compared with healthy controls, which was indicative of aberrant immune activation in RA. This was improved by (S_R)@TM, possibly due to the ability of MET to reduce MHC-II expression levels. Furthermore, because of its exceptional targeting capability and remarkable ability to reduce inflammatory cell recruitment, (S_R)@TM treatment normalized $CD4^+$ T cell counts in rats to a level similar to that in healthy rats (Fig. 8, C and D) (*53*). In rats with AIA, there was a notable decrease in the number of T_{reg} cells and an increase in the number of T_H17 cells, leading to a significant reduction in the T_{reg} cell/T_H17 cell ratio and indicating

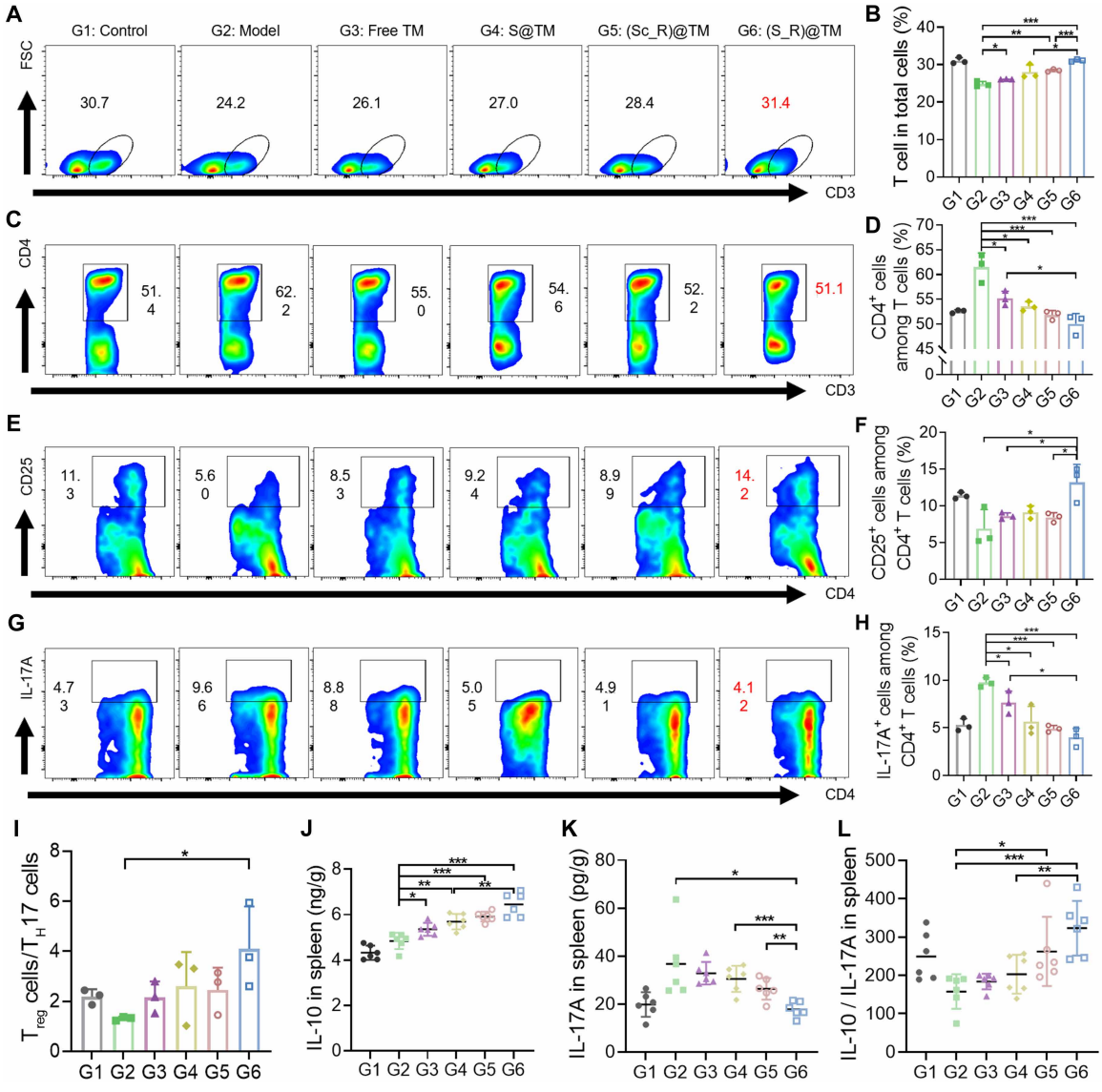

Fig. 8. In vivo immunogenicity of (S_R)@TM. Rate and number of $CD3^+$ cells (**A** and **B**), FSC in (A) defined as forward scatter, $CD4^+$ cells within the $CD3^+$ T cell population (**C** and **D**), regulatory T cells (T_{reg} cells) (**E** and **F**), and T_H17 cells (**G** and **H**) within the $CD4^+$ T cell population were analyzed in the spleen using FCM at day 27 ($n = 3$ biologically independent mice). (**I**) The ratio of T_{reg} cells to T_H17 cells in the spleen ($n = 3$ biologically independent mice). Expression levels of IL-10 (**J**) and IL-17A (**K**) in the spleen on day 27 were analyzed using enzyme-linked immunosorbent assay (ELISA; $n = 6$ biologically independent mice). (**L**) The ratio of IL-10 to IL-17A in the spleen ($n = 6$ biologically independent mice). Treatment groups: G1, control; G2, model; G3, free TM; G4, S@TM; G5, (Sc_R)@TM; G6, (S_R)@TM. Data in [(B), (D), (F), (H), and (I) to (L)] were presented as means ± SD. *P* values were determined by two-sided Student's *t* test. $^*P < 0.05$; $^{**}P < 0.01$; $^{***}P < 0.001$.

immune imbalance. However, treatment, particularly with NP interventions, restored this balance. The T_{reg} cell/T_H17 cell ratio in the NP-treated groups even exceeded that of the healthy controls. This restoration is attributed to the ability of MET to inhibit immune activation and the efficient targeting capabilities of the NPs. Among the NPs, S@TM and (S_R)@TM showed superior regulatory effects to those of (Sc_R)@TM. This suggested that the assembly of NFs may mediate more effective immune regulation by reducing immune cell recruitment through a physical barrier effect (Fig. 8, E to I). As IL-10 and IL-17A serve as markers of T_{reg} and T_H17 cells, respectively, we quantified their expression levels in spleen tissue using enzyme-linked immunosorbent assay (ELISA) (Fig. 8, J to L). These results collectively demonstrated that (S_R)@TM modulated T cell differentiation, thereby alleviating synovium inflammation and T cell activation in rats with AIA and highlighting its potent therapeutic efficacy.

In vivo systemic toxicity evaluation

No hemolysis was observed with any of the concentrations of (S_R)@TM (fig. S24A). Liver and kidney function index concentrations remained within the normal ranges (fig. S24, B to E). No obvious organ damage was observed in H&E-stained sections (fig. S24F), confirming the excellent biocompatibility of all NPs used in this study.

DISCUSSION

Despite advancements in clinical anti-inflammatory therapies for RA, treatment outcomes remain suboptimal. Two factors mainly limit the therapeutic efficacy: The neglect of vascular abnormalities leads to an oversimplified treatment strategy, and the heterogeneous microenvironment of RA lesions impedes effective drug accumulation and precise targeting. To address these challenges, we developed microenvironment-driven transformable self-assembly nanoplatforms, designated as (S_R)@TM.

In RA, the impairment of vasculature contributes to joint inflammation and immune abnormalities, exacerbating disease progression. Consequently, vascular repair and functional normalization constitute pivotal therapeutic targets to reshaping the microenvironment of RA lesions. We strategically used the STP peptide, which undergoes acid-triggered self-assembly into NFs within synovium microenvironment, creating an in situ physical barrier that rapidly inhibits inflammatory cell infiltration (Figs. 4, A to C, and 7, C and D). Furthermore, the NFs exert a pharmacological intervention by disrupting the VEGFR2-VEGF signaling pathway, providing long-term vascular normalization therapeutic effects (Fig. 4D and figs. S11 and S22A). Although the quantitative perivascular distribution of NFs warrants further investigation, the multimodal evaluations spanning cellular to animal models provides robust evidence for both the transient physical barrier effect and sustained regulatory function mediated by the STP NFs. Moreover, the dysregulation of the immune system triggers autoimmune reactions against self-antigens in RA. (S_R)@TM down-regulated the expression of MHC-II and restores the T_{reg} cell/T_H17 cell ratio to normal levels, thereby remodeling the immune landscape (Figs. 4E and 8). In vitro and in vivo studies underscored the immunomodulatory, anti-inflammatory, bone metabolism–regulating, and synovium proliferation–reducing effects of (S_R)@TM (Figs. 6 to 8 and figs. S19 to S22). Thus, (S_R)@TM enables the vascular normalization and intra-articular microenvironment remodeling functions to occur synergistically across multiple spatiotemporal dimensions, remodeling the inflammatory and immune homeostasis.

The morphology and surface modifications of NPs are pivotal in determining their distribution and targeting specificity. (S_R)@TM uses the STP peptide for active targeting of VEGFR2 and undergoing a shape transformation to α helix NFs in the acidic inflammatory synovium microenvironment. In vitro and in vivo experiments confirmed that the physical barrier formed by STP NFs reduces drug leakage in inflamed joints (Figs. 3J and 5). In addition, the S_R modification shielded the positive charge of R@TM NPs and ensured a long life in systemic circulation. Subsequently, excessive MMP2 in RA lesions triggered the separation of STP-GPLG and positively charged VRGD-modified R@TM NPs. R@TM NPs effectively bound to integrin $\alpha_v\beta_3$ via RGD mediation, achieving cascade-targeting and specific localization, facilitating cellular uptake, and synergistically improving drug retention and penetration at RA lesion sites in synergy with NFs (Figs. 2, 3, and 5).

Overall, our findings robustly confirmed that (S_R)@TM exhibited remarkable anti-RA effects underpinned by the proposed microenvironment-driven transformable self-assembly nanoplatforms. By manipulating morphological transformations, strategic charge reversal, and RGD reemergence, (S_R)@TM achieves targeted accumulation at RA lesions. Driven by the unique RA microenvironment, the detached STP-GPLG sequence assembles into NFs that anchor to the vascular endothelium. This process notably enhances NP retention while suppressing inflammatory cell recruitment and angiogenesis. Furthermore, the R@TM NPs deeply penetrated RA lesions, precisely modulating inflammatory responses and antigen presentation. Consequently, (S_R)@TM emerges as a potent system for enhancing spatial multidrug delivery efficiency, offering a pioneering therapeutic strategy for complex autoimmune disorders that may extend beyond RA.

MATERIALS AND METHODS

Materials

Peptides S_R (M_w = 2682.91 Da), S (M_w = 2510.78 Da), Sc_R (M_w = 2793.11 Da), FITC-Acp-S_R (M_w = 3185.45 Da), and FITC-Acp-Sc_R (M_w = 3295.65 Da) were purchased from Dechi Biosciences Co. Ltd. (Shanghai, China). DSPE-PEG_{2000} and DSPE-PEG_{2000}-maleimide were obtained from Ponsure Biotechnology Co. Ltd. (Shanghai, China). TPL was purchased from RENI Pharmaceutical Technology Co. Ltd. (Chengdu, China). 1,1-Dimethylbiguanide hydrochloride (MET) and DiD cell membrane–labeled fluorescent probes were obtained from Solarbio Technology Co. Ltd. (Beijing, China). Dimethyl sulfoxide was purchased from Sigma-Aldrich (St. Louis, MO, USA).

Cell culture

RAW 264.7 cells and L929 cells were obtained from American Type Culture Collection (Manassas, USA). Immortalized synovial fibroblasts from human rheumatic joints were obtained from Yvchi Biology Co. Ltd. (Shanghai, China). Immortalized HUVECs and THP-1 cells were procured from the Chinese Academy of Sciences Cell Bank (Shanghai, China). Cells were cultured in the following media: Dulbecco's modified Eagle's medium (DMEM), Minimum Essential Medium (MEM), or Roswell Park Memorial Institute medium 1640 (RPMI 1640) (all from Gibco, USA), supplemented with 10% fetal bovine serum (FBS; Gibco, USA) and 1% penicillin-streptomycin (PS; Boster Biological Technology Co., Ltd, China). Phosphate-buffered saline (PBS; Servicebio, China) was used for washing, and cell dissociation was performed with 0.25% trypsin-EDTA solution (Gibco, USA). RAW 264.7 cells and HUVECs were incubated in DMEM with 10% FBS and 1% penicillin-streptomycin (PS). L929 cells were cultured in MEM supplemented with 10% FBS and 1% PS. THP-1 cells were cultured in RPMI 1640 supplemented with 10% FBS and 1% PS. All cells were cultured in 37°C in a humidified atmosphere with 5% CO_2. RAW 264.7 cells were differentiated into M1 MØs by activation with LPS (500 ng/ml; Sigma-Aldrich, USA) for 12 hours. To differentiate RAW 264.7 cells into OCs, cells were activated with RANKL (2 ng/ml; Absin, China) for 12 hours. Phycoerythrin (PE)-labeled $\alpha_v\beta_3$ antibodies (Santa Cruz Biotechnology, catalog no. sc-7312) were used to confirm the successful differentiation of M1 MØs and OCs. HUVECs were activated with TNF-α (10 ng/ml; UA Biotech, China). PE-labeled VEGFR2 antibodies (BD Biosciences, catalog no. 560494) were used to verify the increased expression of VEGFR2 following induction. For the establishment of an in vitro vascular model, HUVECs were seeded on the transwell chamber (Corning, China) at 5×10^5 per well and activated with TNF-α until a dense cell layer formed on the polyethylene terephthalate (PET) membrane.

Animal care

Male Sprague-Dawley rats (160 to 180 g) were obtained from SPF biotechnology Co. Ltd. (Beijing, China). Animals were acclimatized for 1 week before experiments with a fresh diet and water ad libitum.

All animal experiments were approved by Ethical Review Committee and Laboratory Animal Welfare Committee of Chengdu University of Traditional Chinese Medicine. Animal welfare was ensured during whole animal experiments.

Synthesis and characterization of S_R-PEG$_{2000}$-DSPE

S_R-PEG$_{2000}$-DSPE was synthesized via Michael addition. Briefly, Mal-PEG$_{2000}$-DSPE and S_R-Cys (molar ratio = 3: 2) were reacted in a solvent mixture of chloroform/methanol (MeOH) (v/v = 4 : 1) with gentle stirring at room temperature for 24 hours. The solvent was evaporated under vacuum to obtain S_R-PEG$_{2000}$-DSPE. Similar procedures were followed for S-PEG$_{2000}$-DSPE, Sc_R-PEG$_{2000}$-DSPE, FITC-Sc_R-PEG$_{2000}$-DSPE, and FITC-S_R-PEG$_{2000}$-DSPE using appropriate starting materials (S-Cys, Sc_R-Cys, FITC-Sc_R-Cys, FITC-S_R-Cys, and Mal-PEG$_{2000}$-DSPE). Successful synthesis was confirmed by MALDI-TOF-MS (Axima Performance; Shimadzu, China).

Preparation and characterization of (S_R)@TM

(S_R)@TM was prepared via ultrasonic-emulsification. Briefly, S_R-PEG$_{2000}$-DSPE and TPL were dissolved in 0.25 ml of a solvent mixture (chloroform/MeOH, v/v = 4 : 1) to form the oil phase, while MET was dissolved in 1 ml of PBS to form the aqueous phase. The oil and water phases were mixed and emulsified using a probe sonicator. After evaporating the organic solvent under reduced pressure, (S_R)@TM was obtained. S@TM and (Sc_R)@TM were prepared similarly using S-PEG$_{2000}$-DSPE and Sc_R-PEG$_{2000}$-DSPE, respectively. Hydrophobic fluorescent dye DiD-loaded and Rh B–loaded NPs (pep@TM$_{DiD}$ and pep@TM$_{Rh\ B}$) were prepared by incorporating DiD into the oil phase and Rh B into the aqueous phase, following the same procedure. FITC-labeled S_R and Sc_R were incorporated into NP formulations, designated as (S_R)$_{FITC}$@TM and (Sc_R)$_{FITC}$@TM, respectively.

The particle sizes, PDI, and zeta potentials of (S_R)@TM, S@TM, and (Sc_R)@TM were determined by dynamic light scattering (DLS) using a Zetasizer Nano ZS90 instrument (Malvern Panalytical, UK). The morphology of these NPs was examined by TEM (FEl Tecnai G2 12; Thermo Fisher Scientific, USA). To evaluate serum stability, (S_R)@TM was incubated in 10% FBS PBS or PBS at 37°C for 24 hours, and changes in particle sizes were monitored using DLS. PBS at 4°C for 72 hours was used as a control.

Bioinformatic analysis

Bioinformatics investigation of the synovial tissue transcriptomes used RNA sequencing data sourced from the publicly accessible GSE89408 dataset. This dataset encompassed samples from patients with RA, who were diagnosed within the preceding 12-month period and had not received any prior treatment, as well as healthy control subjects. The differential gene expression analysis was conducted using the Wilcoxon rank sum test.

MMP2 and pH responsiveness

The (S_R)@TM formulation pH was adjusted to 5.8, followed by addition of recombinant human MMP2 (Peprotech, USA) to achieve a final concentration of 0.25 μg/ml. Subsequently, these samples were incubated at 37°C for 12 hours, and the particle size and PDI of each group were determined using DLS. TEM was used to observe the morphology, while MALDI-TOF-MS analyzed changes in molecular weight. Moreover, to verify assembly of NFs under acidic conditions, (S_R)@TM was incubated with MMP2 in acidic condition with circular dichroism (CD) spectrum validation α helix structure. (S_R)@TM or (Sc_R)@TM were incubated under varying conditions. The detached STP/Sc-GPLG fragments were then purified using Dextran Gel G-50 (Solarbio, China) and quantified via spectrophotometry. After incubation and dialysis of (S_R)@TM under different conditions, quantitative analysis of TPL and MET was performed using a ultraviolet spectrophotometer. Peptide cleavage was assessed by observing the FRET effect. In brief, after incubating the (S_R)$_{FITC}$@TM$_{Rh\ B}$ and (Sc_R)$_{FITC}$@TM$_{Rh\ B}$ with MMP2 for 12 hours, it was incubated with FITC equivalents (10 μg/ml) with HUVECs in basic culture medium at pH 5.8 for 2 hours, and, then, only the FITC excitation light was excited by confocal laser scanning microscope (TCS SP8 STED; Leica, German) to observe Rh B.

In vitro–targeted assessment

The structure of the VEGFR2-VEGFA protein complex is sourced from the Protein Data Bank database (www1.rcsb.org/). The binding site of the peptide (SKDEEWHKNNFPLSP, STP) to the VEGFR2 protein was calculated using the AlphaFold3 online tool for protein structure prediction https://alphafoldserver.com/welcome). Activated HUVECs were seeded in glass-bottomed dishes treated with (S_R)$_{FITC}$@TM$_{DiD}$ and (Sc_R)$_{FITC}$@TM$_{DiD}$ [with or without MMP2 (0.25 μg/ml)] in the serum-free medium. After 3 hours of incubation, cells were fixed, stained with 4′,6-diamidino-2-phenylindole (DAPI), and imaged using CLSM. Additionally, cells seeded in the upper chamber of the transwell were treated similarly, and, after 3 hours, membranes with cells were fixed, stained with DAPI, and imaged in three-dimensional fluorescence using CLSM. The VEGFR2 targeting efficiency was quantified by seeding cells in 24-well plates, treating them as described, and measuring FITC and DiD fluorescence intensities using a flow cytometer (BD FACS Celesta, USA) after 3 hours of incubation. Flow cytometric data were analyzed with FlowJo V10 software.

M1 MØs, OCs, and HRAFLS were seeded in 24-well plates and treated with various DiD-loaded NPs for 3 hours. Cells were then collected, and DiD fluorescence intensity was measured by FCM. For qualitative analysis of cell uptake, M1 MØs, OCs, and HRAFLS were seeded in a glass-bottom lower transwell chamber of in vitro vascular model. NPs were introduced in serum-free medium containing MMP2 (0.25 μg/ml) and incubated with the in vitro vascular model. After 12 hours, cells were fixed, stained with DAPI, and imaged. DiD fluorescence intensity was achieved using LAS X software.

Reduced angiogenesis and adhesion of THP-1

Activated HUVECs were resuspended in various NP formulations and seeded at a density of 3×10^4 per well in 96-well plates coated with 50 μl of Matrigel (Corning, China). Cell morphology was observed under a microscope at 6- and 10-hour intervals. Upon successful establishment of the in vitro vascular model, different NPs groups were introduced into the serum-free medium in the upper chamber. After 3 and 12 hours of incubation, THP-1 cells marked with CMFDA were seeded at 3×10^5 cells per well. Following 3 hours of incubation period, PET membranes with adherent cells were fixed after washing with PBS. Three-dimensional fluorescence images of the membranes were captured using CLSM. Semiquantitative analysis of THP-1 cells was achieved using ImageJ software.

Reduce MHC-II and CD86 expression in LPS-activated RAW 264.7 cells

M1 MØs were seeded in 24-well plates. Following different treatments for 12 hours, PE-labeled MHC-II antibodies (Abcam, China) or APC-labeled CD86 antibodies (Thermo Fisher Scientific, USA) were incubated with harvested cells for 15 min. The levels of MHC-II and CD86 expression were quantified using FCM.

Cytotoxicity study

M1 MØs, OCs, and HRAFLS were treated with various NPs (equivalent to 20 ng/ml TPL, with MMP2 pretreatment) for 24 hours. Cell viability was assessed using the CCK8 assay kit (Bioground, China) following the manufacturer's protocol. Cell apoptosis was evaluated using an Annexin V-FITC Apoptosis/Propidium Iodide Detection Kit (Beyotime, China) according to the manufacturer's instructions.

Effect of OC differentiation and bone resorption

OCs were treated with different NPs (equivalent to TPL at 20 ng/ml and MMP2 at 0.25 μg/ml) for 24 hours, with an untreated group serving as a control. At the experimental end point, cells were stained using the TRAP Stain Kit (Solarbio, China) and observed under light microscopy. RAW 264.7 cells were seeded onto 96-well plates containing bovine cortical bone slices for 12 hours, followed by treatment with culture medium containing RANKL and various NPs. After 48 hours, absorption pits were stained with benzylamine blue (Solarbio, China), visualized as dark blue pits under light microscopy, and quantified.

Establish AIA model

Healthy male SD rats received subcutaneously injected with Freund's adjuvant (50 μl) containing heat-killed mycobacteria (10 mg/ml; Chondrex, Washington DC, USA) into the right hindlimb paw. The arthritis rat model was successfully induced 14 days post–disease initiation. Immunohistochemical staining for MMP2 (Proteintech Group, catalog no. 10373-2-AP), VEGFR2 (Cell Signaling Technology, catalog no. 9698), and $\alpha_v\beta_3$ (Santa Cruz Biotechnology, catalog no. sc-7312) in synovial tissues of the knee joint was performed to validate the successful establishment of the model.

Biodistribution

AIA rats were established and intravenously injected with free DiD, S@TM_{DiD}, (Sc_R)@TM_{DiD}, and (S_R)@TM_{DiD} at a DiD dose of 20 μg/kg. In vivo imaging analysis of DiD fluorescence using an IVIS was conducted at 4, 10, 24, 36, and 48 hours postinjection to track biodistribution. Rats were euthanized at 48 hours, and organs (heart, liver, spleen, lung, kidney) and ankle joints were collected for ex vivo imaging of DiD fluorescence. Semiquantitative analysis was performed using region-of-interest analysis.

Immunofluorescence staining

AIA rats were intravenously injected with $(S\_R)_{FITC}$@TM_{DiD} or $(Sc\_R)_{FITC}$@TM_{DiD}. Synovium of right leg knee joint were collected 36 hours postinjection and sectioned to 15-μm thickness. Tissue sections were first incubated with primary antibodies against CD31 (rabbit recombinant multiclonal, Abcam, catalog no. ab281583) or LYVE-1 (rabbit polyclonal, Thermo Fisher Scientific, catalog no. PA1-16635). Then, sections were incubated with Cy3-conjugated secondary antibody (Biodragon, Catalog BD9724). Nuclei were subsequently counterstained with DAPI. Fluorescent distributions in synovium joints were observed using a laser scanning confocal microscope (Leica M205 FA). Colocalization analyses were performed for FITC with blood vessels, DiD with blood vessels, and DiD with lymphatics. Colocalization analysis was performed using HALO (v3.60) system and ImageJ software.

Anti-RA treatment of (S_R)@TM in vivo

AIA rats were randomly divided into six groups, including the control group, the model group receiving PBS, the free drug group (TPL, MET, and peptides at equivalent concentrations as NPs), the S@TM group, the (Sc_R)@TM group, and (S_R)@TM group at an identical dose of TPL (100 μg/kg), MET, and peptides ($n = 7$). Furthermore, some healthy rats without Freund's complete adjuvant treatment served as the normal control. Injections were given every other day for a total of seven injections. The body weight, paw thickness, and ankle diameter of the rats were measured every other day, and the joints were observed and scored scientifically. On the 27th day after the induction of arthritis, whole blood was collected from abdominal aorta of each group and centrifuged at 4°C and 3000 rpm for 15 min to obtain the upper serum used to determine liver and renal function. The right ankle joints, synovium, main organs (heart, liver, spleen, lung, and kidney) of euthanized rats were collected and then fixed by 4% paraformaldehyde. The paws were cut off from the ankle joint were fixed with formalin. Rat paw scoring was performed on a 0-4 scale given by a blinded researcher based on the following criteria: in each rat paw, where 0 indicated no swelling or erythema; 1 indicated slight swelling or erythema on the soles of the feet and slight redness on the ankles; 2 indicated mild swelling and slight ulceration of the sole, along with mild to moderate edema of the ankle joint; 3 indicated moderate edema and ulceration on the sole of the foot, with limited ankle movement; and 4 indicated severe edema and ulceration of the soles of the feet accompanied by ankle stiffness.

Radiologic and histopathological analysis

The right hind paws of rats from different experimental groups were fixed in 4% paraformaldehyde and subjected to micro-CT imaging using a system from PerkinElmer Inc. (USA). Three-dimensional reconstructions were generated and analyzed. The bone erosion of each rat were blindly scored according to the radiographs, scoring was arranged on a 0-4 scale in each rat paw, where 0 indicated smooth articular surface, no marginal osteophyte, normal articular cavity, good correspondence between interphalangeal joint and metatarsophalangeal joint; 1 indicated slight articular surface roughness, less marginal osteophyte, slightly narrowed articular cavity; 2 indicated low-to-moderate articular surface roughness, low-to-moderate marginal osteophyte, low-to-moderate narrowed articular cavity; 3 indicated pronounced articular surface roughness, pronounced marginal osteophyte, narrowed articular cavity; and 4 indicated serious articular surface roughness, serious marginal osteophyte, serious narrowed articular cavity, terrible correspondence between interphalangeal joint and metatarsophalangeal joint. The highest radiological score up to 4 for each rat. Synovium and major organ tissues were stained with H&E to assess histological changes. Synovium blood capillaries were immunostained using CD31 antibody (Servicebio, catalog no. GB11063-2), OCs were visualized with CD51 antibody (Servicebio, catalog no. GB11293-2), and cell-to-cell junctions were visualized using ZO-1 antibodies (Proteintech Group, catalog no. 21773-1-AP). Semiquantitative analysis of immunohistochemistry was achieved by HALO (v3.60) system.

Ex vivo analysis of immune cell distribution and activation in synovium and spleen

Synovium tissues were harvested from rats in each experimental group and stained with antibodies targeting established immune cell biomarkers and representative extracellular matrix components, following the manufacturer's protocols. Semiquantitative analysis of fluorescence was achieved by HALO (v3.60) system. Rat spleen cells were analyzed by FCM to identify immune cell types. Specific antibodies are included: representative extracellular matrix components (aggrecan, Proteintech Group, catalog no. 13880-1-AP); T cells (anti-CD3, Servicebio, catalog no. GB12014; anti-CD3-FITC, BD, catalog no. 559975; anti-CD4-APC, BD, catalog no. 550057; anti-CD4, Servicebio, catalog no. GB15064); MØs (anti-CD86, Bioss, catalog no. bsm-52375R; anti-CD206, Abcam, catalog no. ab64693); neutrophils (anti-Ly6G, Servicebio, catalog no. GB11224); monocytes (anti-CD14, Servicebio, catalog no. GB11254); T_{reg} cells (anti-CD25-BV421, BD, catalog no. 565608; anti-FOXP3, Servicebio, catalog no. GB112325); and T_H17 cells (anti–IL-17A–PE–Cy7, eBioscience, catalog no. 25-7177-82; anti–IL-17A, Servicebio, catalog no. GB11110-1). Furthermore, IL-10 and IL-17A levels in the spleen were quantified using ELISA kits from Thermo Fisher Scientific Co. Ltd., following the manufacturer's instructions.

Statistical analysis

Statistical analyses were performed using Prism software (version 9.0, GraphPad Software). Data reported as the means ± SD. Two-tailed Student's *t* test was applied to test the statistical significance of differences between two groups. Statistical significance was defined as $^*P < 0.05$, $^{**}P < 0.01$, and $^{***}P < 0.001$.

Supplementary Materials

The PDF file includes:
Figs. S1 to S24
Legend for table S1

Other Supplementary Material for this manuscript includes the following:
Table S1

REFERENCES AND NOTES

1. C. A. Dinarello, Anti-inflammatory agents: Present and future. *Cell* **140**, 935–950 (2010).
2. G. Schett, E. Gravallese, Bone erosion in rheumatoid arthritis: Mechanisms, diagnosis and treatment. *Nat. Rev. Rheumatol.* **8**, 656–664 (2012).
3. Z. Chen, A. Bozec, A. Ramming, G. Schett, Anti-inflammatory and immune-regulatory cytokines in rheumatoid arthritis. *Nat. Rev. Rheumatol.* **15**, 9–17 (2019).
4. J. Li, M. Zhang, J. Shi, S. Wang, X. Zhong, Y. Wu, Y. Qu, H. Gao, J. Zhang, pH-sensitive nano-polyelectrolyte complexes with arthritic macrophage-targeting delivery of triptolide. *Int. J. Pharm.* **632**, 122572 (2023).
5. T. Wang, C. Huang, Z. Fang, A. Bahatibieke, D. Fan, X. Wang, H. Zhao, Y. Xie, K. Qiao, C. Xiao, Y. Zheng, A dual dynamically cross-linked hydrogel promotes rheumatoid arthritis repair through ROS initiative regulation and microenvironment modulation-independent triptolide release. *Mater. Today Bio* **26**, 101042 (2024).
6. J. D. Schwartz, S. Monea, S. G. Marcus, S. Patel, K. Eng, A. C. Galloway, P. Mignatti, P. Shamamian, Soluble factor(s) released from neutrophils activates endothelial cell matrix metalloproteinase-2. *J. Surg. Res.* **76**, 79–85 (1998).
7. K. Ley, C. Laudanna, M. I. Cybulsky, S. Nourshargh, Getting to the site of inflammation: The leukocyte adhesion cascade updated. *Nat. Rev. Immunol.* **7**, 678–689 (2007).
8. E. Nevius, A. C. Gomes, J. P. Pereira, Inflammatory cell migration in rheumatoid arthritis: A comprehensive review. *Clin. Rev. Allergy Immu.* **51**, 59–78 (2016).
9. G. Dunlap, A. Wagner, N. Meednu, R. Wang, F. Zhang, J. C. Ekabe, A. H. Jonsson, K. Wei, S. Sakaue, A. Nathan, V. P. Bykerk, L. T. Donlin, S. M. Goodman, G. S. Firestein, D. L. Boyle, V. M. Holers, L. W. Moreland, D. Tabechian, C. Pitzalis, A. Filer, S. Raychaudhuri, M. B. Brenner, J. Thakar, A. McDavid, D. A. Rao, J. H. Anolik, Clonal associations between lymphocyte subsets and functional states in rheumatoid arthritis synovium. *Nat. Commun.* **15**, 4991 (2024).
10. T. E. Sutherland, D. P. Dyer, J. E. Allen, The extracellular matrix and the immune system: A mutually dependent relationship. *Science* **379**, eabp8964 (2023).
11. H. Mei, S. Cai, D. Huang, H. Gao, J. Cao, B. He, Carrier-free nanodrugs with efficient drug delivery and release for cancer therapy: From intrinsic physicochemical properties to external modification. *Bioact. Mater.* **8**, 220–240 (2022).
12. S. Shin, B. Hyun, A. Lee, H. Kong, S. Han, C. K. Lee, N. J. Ha, K. Kim, Metformin suppresses MHC-restricted antigen presentation by inhibiting co-stimulatory factors and MHC molecules in APCs. *Biomol. Ther.* **21**, 35–41 (2013).
13. D. Liang, L. Liu, Y. Qi, F. Nan, J. Huang, S. Tang, J. Tang, N. Chen, Jin-Gui-Shen-Qi Wan alleviates fibrosis in mouse diabetic nephropathy via MHC class II. *J. Ethnopharmacol.* **324**, 117745 (2024).
14. L. Klareskog, A. I. Catrina, S. Paget, Rheumatoid arthritis. *Lancet* **373**, 659–672 (2009).
15. A. de Vere Tyndall, S. C. Knight, A. J. Edwards, J. B. Clarke, Veiled (dendritic) cells in synovial fluid. *Lancet* **1**, 472–473 (1983).
16. I. B. McInnes, G. Schett, The pathogenesis of rheumatoid arthritis. *N. Engl. J. Med.* **365**, 2205–2219 (2011).
17. N. Komatsu, S. Win, M. Yan, N. C.-N. Huynh, S. Sawa, M. Tsukasaki, A. Terashima, W. Pluemsakunthai, G. Kollias, T. Nakashima, H. Takayanagi, Plasma cells promote osteoclastogenesis and periarticular bone loss in autoimmune arthritis. *J. Clin. Invest.* **131**, 143060 (2021).
18. W. Zhang, Y. Chen, Q. Liu, M. Zhou, K. Wang, Y. Wang, J. Nie, S. Gui, D. Peng, Z. He, Z. Li, Emerging nanotherapeutics alleviating rheumatoid arthritis by readjusting the seeds and soils. *J. Control. Release* **345**, 851–879 (2022).
19. H. Cabral, J. Li, K. Miyata, K. Kataoka, Controlling the biodistribution and clearance of nanomedicines. *Nat. Rev. Bioeng.* **2**, 214–232 (2024).
20. N. Honkura, M. Richards, B. Laviña, M. Sáinz-Jaspeado, C. Betsholtz, L. Claesson-Welsh, Intravital imaging-based analysis tools for vessel identification and assessment of concurrent dynamic vascular events. *Nat. Commun.* **9**, 2746 (2018).
21. X. Qin, L. Pan, T. Chen, D. Li, X. Lin, G. Li, C. Feng, W. Ye, W. Liang, J. Chen, Q. Wang, Inflammation-responsive nanoparticles suppress lymphatic clearance for prolonged arthritis therapy. *J. Control. Release* **352**, 700–711 (2022).
22. P. Carmeliet, R. K. Jain, Principles and mechanisms of vessel normalization for cancer and other angiogenic diseases. *Nat. Rev. Drug Discov.* **10**, 417–427 (2011).
23. P. Bhattarai, S. Hameed, Z. Dai, Recent advances in anti-angiogenic nanomedicines for cancer therapy. *Nanoscale* **10**, 5393–5423 (2018).
24. A. N. Lyle, W. R. Taylor, The pathophysiological basis of vascular disease. *Lab. Invest.* **99**, 284–289 (2019).
25. Y. Qian, W. Wang, Z. Wang, Q. Han, X. Jia, S. Yang, Z. Hu, Switchable probes: pH-triggered and VEGFR2 targeted peptides screening through imprinting microarray. *Chem. Commun.* **52**, 5690–5693 (2016).
26. Q. Han, W. Wang, X. Jia, Y. Qian, Q. Li, Z. Wang, W. Zhang, S. Yang, Y. Jia, Z. Hu, Switchable liposomes: Targeting-peptide-functionalized and pH-triggered cytoplasmic delivery. *ACS Appl. Mater. Interfaces* **8**, 18658–18663 (2016).
27. Y. Kuang, J. Shi, J. Li, D. Yuan, K. A. Alberti, Q. Xu, B. Xu, Pericellular hydrogel/nanonets inhibit cancer cells. *Angew. Chem. Int. Ed. Engl.* **53**, 8104–8107 (2014).
28. C. Zhang, L.-H. Liu, W.-X. Qiu, Y.-H. Zhang, W. Song, L. Zhang, S.-B. Wang, X.-Z. Zhang, A transformable chimeric peptide for cell encapsulation to overcome multidrug resistance. *Small* **14**, e1703321 (2018).
29. L. Zhang, Z. Jiang, X. Yang, Y. Qian, M. Wang, S. Wu, L. Li, F. Jia, Z. Wang, Z. Hu, M. Zhao, X. Tang, G. Li, H. Shang, X. Chen, W. Wang, A totipotent "all-in-one" peptide sequentially blocks immune checkpoint and reverses the immunosuppressive tumor microenvironment. *Adv. Mater.* **35**, e2207330 (2023).
30. M. Simons, E. Gordon, L. Claesson-Welsh, Mechanisms and regulation of endothelial VEGF receptor signalling. *Nat. Rev. Mol. Cell Biol.* **17**, 611–625 (2016).
31. Z. Liao, T. Liu, Z. Yao, T. Hu, X. Ji, B. Yao, Harnessing stimuli-responsive biomaterials for advanced biomedical applications. *Exploration* **5**, 20230133 (2025).
32. R. Liang, Y. Tu, P. Hua, Y. Huang, M. Chen, ROS-responsive micelles co-loaded dexamethasone and pristimerin to restore the homeostasis of the inflammatory microenvironment for rheumatoid arthritis therapy. *Chin. Chem. Lett.* **36**, 110335 (2025).
33. M. Zhang, W. Hu, C. Cai, Y. Wu, J. Li, S. Dong, Advanced application of stimuli-responsive drug delivery system for inflammatory arthritis treatment. *Mater. Today Bio.* **14**, 100223 (2022).
34. Y. H. Chang, I. L. Lin, G. J. Tsay, S. C. Yang, T. P. Yang, K. T. Ho, T. C. Hsu, M. Y. Shiau, Elevated circulatory MMP-2 and MMP-9 levels and activities in patients with rheumatoid arthritis and systemic lupus erythematosus. *Clin. Biochem.* **41**, 955–959 (2008).
35. C. Deng, Q. Zhang, P. He, B. Zhou, K. He, X. Sun, G. Lei, T. Gong, Z. Zhang, Targeted apoptosis of macrophages and osteoclasts in arthritic joints is effective against advanced inflammatory arthritis. *Nat. Commun.* **12**, 2174 (2021).
36. W. Jia, B. Gong, J. Chen, J. Yan, Y. Shi, H. Wang, M. Qin, H. Gao, Dual-responsive shape-transformable charge-reversible nanoparticles combined with chemo-

photodynamic-immunotherapy for the treatment of breast cancer and lung metastasis. *Adv. Funct. Mater.* **34**, 2408581 (2024).
37. X. Chen, L. Liu, C. Jiang, Charge-reversal nanoparticles: Novel targeted drug delivery carriers. *Acta Pharm. Sin. B* **6**, 261–267 (2016).
38. D. Wei, K. Pang, Q. Song, Y. Suo, H. He, X. Weng, X. Gao, X. Wei, Noninvasive monitoring of nanoparticle clearance and aggregation in blood circulation by in vivo flow cytometry. *J. Control. Release* **278**, 66–73 (2018).
39. A. R. Motezakker, L. G. Greca, E. Boschi, G. Siqueira, F. Lundell, T. Rosén, G. Nyström, L. D. Söderberg, Stick, slide, or bounce: Charge density controls nanoparticle diffusion. *ACS Nano* **18**, 28636–28648 (2024).
40. P. Joyce, C. J. Allen, M. J. Alonso, M. Ashford, M. S. Bradbury, M. Germain, M. Kavallaris, R. Langer, T. Lammers, M. T. Peracchia, A. Popat, C. A. Prestidge, C. J. F. Rijcken, B. Sarmento, R. B. Schmid, A. Schroeder, S. Subramaniam, C. R. Thorn, K. A. Whitehead, C. X. Zhao, H. A. Santos, A translational framework to DELIVER nanomedicines to the clinic. *Nat. Nanotechnol.* **19**, 1597–1611 (2024).
41. Q. Han, X. Jia, Y. Qian, Z. Wang, S. Yang, Y. Jia, W. Wang, Z. Hu, Peptide functionalized targeting liposomes: For nanoscale drug delivery towards angiogenesis. *J. Mater. Chem. B* **4**, 7087–7091 (2016).
42. R. Brusini, M. Varna, P. Couvreur, Advanced nanomedicines for the treatment of inflammatory diseases. *Adv. Drug Deliv. Rev.* **157**, 161–178 (2020).
43. S. Li, J. Li, Y. Zhao, M. Chen, S. Su, S. Yao, Z. Wang, X. Hu, W. Geng, W. Wang, K. Wang, D. Guo, Supramolecular integration of multifunctional nanomaterial by mannose-decorated azocalixarene with ginsenoside Rb1 for synergistic therapy of rheumatoid arthritis. *ACS Nano* **17**, 25468–25482 (2023).
44. R. T. Meehan, E. A. Regan, E. D. Hoffman, M. L. Wolf, M. T. Gill, J. L. Crooks, P. J. Parmar, R. A. Scheuring, J. C. Hill, K. A. Pacheco, V. Knight, Synovial fluid cytokines, chemokines and MMP levels in osteoarthritis patients with knee pain display a profile similar to many rheumatoid arthritis patients. *J. Clin. Med.* **10**, 5027 (2021).
45. Y. Yoshihara, H. Nakamura, K. Obata, H. Yamada, T. Hayakawa, K. Fujikawa, Y. Okada, Matrix metalloproteinases and tissue inhibitors of metalloproteinases in synovial fluids from patients with rheumatoid arthritis or osteoarthritis. *Ann. Rheum. Dis.* **59**, 455–461 (2000).
46. U. Fearon, M. M. Hanlon, A. Floudas, D. J. Veale, Cellular metabolic adaptations in rheumatoid arthritis and their therapeutic implications. *Nat. Rev. Rheumatol.* **18**, 398–414 (2022).
47. B. Ramamurthi, Treatment of osteoarthritis with intra-articular injections of lactic acid. *Ind. Med. Gaz.* **82**, 264–265 (1947).
48. L. Liu, F. Hu, H. Wang, X. Wu, A. S. Eltahan, S. Stanford, N. Bottini, H. Xiao, M. Bottini, W. Guo, X. J. Liang, Secreted protein acidic and rich in cysteine mediated biomimetic delivery of methotrexate by albumin-based nanomedicines for rheumatoid arthritis therapy. *ACS Nano* **13**, 5036–5048 (2019).
49. R. Deng, Y. Bu, F. Li, H. Wu, Y. Wang, W. Wei, The interplay between fibroblast-like synovial and vascular endothelial cells leads to angiogenesis via the sphingosine-1-phosphate-induced RhoA-F-Actin and Ras-Erk1/2 pathways and the intervention of geniposide. *Phytother. Res.* **35**, 5305–5317 (2021).
50. P. B. Narasimhan, P. Marcovecchio, A. A. J. Hamers, C. C. Hedrick, Nonclassical monocytes in health and disease. *Annu. Rev. Immunol.* **37**, 439–456 (2019).
51. A. Marrelli, P. Cipriani, V. Liakouli, F. Carubbi, C. Perricone, R. Perricone, R. Giacomelli, Angiogenesis in rheumatoid arthritis: A disease specific process or a common response to chronic inflammation? *Autoimmun. Rev.* **10**, 595–598 (2011).
52. W. Wj, S. Pa, N. Wb, F. Dm, Intraarticular volume and clearance in human synovial effusions. *Arthritis Rheumatol.* **28**, 441–449 (1985).
53. L. Zhang, Z. Qin, H. Sun, X. Chen, J. Dong, S. Shen, L. Zheng, N. Gu, Q. Jiang, Nanoenzyme engineered neutrophil-derived exosomes attenuate joint injury in advanced rheumatoid arthritis via regulating inflammatory environment. *Bioact. Mater.* **18**, 1–14 (2022).

Acknowledgments
Funding: This work was supported by the National Natural Science Foundation of China (no. 81973662, J.Z.; and no. 82404547, C.H.), National Interdisciplinary Innovation Team of Traditional Chinese Medicine (no. ZYYCXTD-D-202209, J.Z.), Central Guidance on Local Science and Technology Development Fund of Sichuan (no. 23ZYZYTS0420, J.Z.), and Postdoctoral Fellowship Program of CPSF (no. GZC20230333, C.H.). **Author contributions:** Conceptualization: J.Z., C.H., H.G., and J.M. Funding Acquisition: J.Z. and C.H. Methodology: J.Z., C.H., and J.M. Investigation: C.H., J.M., Y.C., X.C., Y.S., Q.T., and X.H. Visualization: C.H., J.M., X.C., and Y.C. Resources: C.H., J.Z., and H.G. Supervision: J.Z., C.H., H.G., and Y.W. Writing—original draft: C.H., J.M., and X.C. Writing—review and editing: J.Z., C.H., and H.G. **Competing interests:** The authors declare that they have no competing interests. **Data and materials availability:** All data needed to evaluate the conclusions in the paper are present in the paper and/or the Supplementary Materials. All raw data for this research are included as an Excel file: table S1.

Submitted 12 November 2024
Accepted 6 August 2025
Published 3 September 2025
10.1126/sciadv.adu5245